# Long Hole Film Cooling Dataset for CFD Development - Flow and Film Effectiveness

Vikram Shyam and Phillip Poinsatte
*NASA Glenn Research Center*
*21000 Brookpark Rd, Cleveland, OH 44135*
*vikram.shyam-1@nasa.gov*

Douglas Thurman
*Army Research Lab/NASA Glenn Research Center*
*21000 Brookpark Rd, Cleveland, OH 44135*

Ali Ameri
*The Ohio State University/NASA Glenn Research Center*
*21000 Brookpark Rd, Cleveland, OH 44135*

**Abstract**

An experiment investigating flow and heat transfer of long (length to diameter ratio of 18) cylindrical film cooling holes has been completed. In this paper, the thermal field in the flow and on the surface of the film cooled flat plate is presented for nominal freestream turbulence intensities of 1.5 and 8 percent. The holes are inclined at 30° above the downstream direction, injecting chilled air of density ratio 1.0 onto the surface of a flat plate. The diameter of the hole is 0.75 in. (~0.02 m) with center to center spacing (pitch) of 3 hole diameters. Coolant was injected into the mainstream flow at nominal blowing ratios of 0.5, 1.0, 1.5, and 2.0. The Reynolds number of the freestream was approximately 11,000 based on hole diameter. Thermocouple surveys were used to characterize the thermal field. Infrared thermography was used to determine the adiabatic film effectiveness on the plate. Hotwire anemometry was used to provide flowfield physics and turbulence measurements. The results are compared to existing data in the literature. The aim of this work is to produce a benchmark dataset for Computational Fluid Dynamics (CFD) development to eliminate the effects of hole length to diameter ratio and to improve resolution in the near-hole region. In this report, a Time Filtered Navier Stokes (TFNS), also known as Partially Resolved Navier Stokes (PRNS), method that was implemented in the Glenn-HT code is used to model coolant-mainstream interaction. This method is a high fidelity unsteady method that aims to represent large scale flow features and mixing more accurately.

## II. Introduction

Gas turbine engines produce thrust by burning fuel in the combustor and accelerating fluid through the engine. To burn efficiently in the combustor, air entering the engine inlet must be compressed to a high pressure ratio. The fluid exiting the combustor can reach temperatures well in excess of the component thermal limits in the high pressure turbine (HPT) section. High operating pressure ratios as well as increased turbine inlet total temperatures are expected to be the hallmarks of NASA's N+3 engines. In order to cool the surfaces of components in the HPT, part of the air form the compressor is bled away and fed through internal passages to the HPT where the relatively cooler fluid is injected through discrete holes onto the surface of the hot components. This cooling fluid is deprived of passage through the combustor and moreover, when fed into the rotor, has work done on it by the rotor instead of being used to turn the HPT blades. In general, an increase in compressor pressure ratio leads to higher engine efficiency. This is accompanied by an increase in the temperature exiting the combustor and entering the high pressure turbine.

The motivation, then, of improving our understanding of film cooling (or thermal management in general) is to reduce the amount of coolant required to cool the surface of the hot components in the HPT by using it more efficiently and by understanding the optimal locations and quantities in which to distribute it. This is accomplished through experiment and CFD. Experiments allow testing of new cooling concepts and serve as benchmarks to

compare computations to. Traditionally, computations have a tendency to under predict laterally averaged film cooling effectiveness data even for the simple case of a flat plate with a cooling hole. There are large errors associated with measurement techniques either due to small temperature gradients or invasive measurement methods. The experimental and computational uncertainty leads to excess coolant being used as a safety margin. Up to 20 percent excess cooling can be used over the mission of an aircraft jet engine. Presently, the cooling air used to cool turbine components comprises approximately 12 percent of the mass flow through the core. It is therefore important to perform simple experiments that isolate the various parameters that have an impact on film cooling to enable development of turbulence modeling that better predicts the physics of the flow and therefore the laterally averaged film cooling effectiveness. The parameters of note for flat plate film cooling using cylindrical holes are injection angle ($\alpha$), blowing ratio (M), density ratio (DR), free stream turbulence intensity ($Tu$), surface roughness, length to diameter ratio (L/D) of the hole and hole spacing (pitch to diameter ratio, P/D). The blowing ratio is a ratio of coolant mass flow rate per unit area to freestream mass flow rate per unit area. The density ratio is the ratio of coolant to freestream density. The hole diameter is D or d. In addition, the manner in which the flow enters the cooling hole plays a significant role in determining the film effectiveness. For example, flow may enter the hole from a plenum in which case the direction of the flow in the plenum is important (same direction as free stream or at an angle to free stream.)

Turbine blades often have compound angled holes although these are angled so that locally they are in the direction of the free stream so as to minimize loss. Typically turbine blades use holes inclined at 30° to 35° to the local freestream and have L/D values ranging from 2 to 4. Blowing ratios are typically high and can approach 2.0 near the leading edge and on the suction side. The density ratios are typically around 2.0 due to the large temperature difference between coolant and freestream. Higher density ratio coolant jets can stay attached at larger blowing ratios due to their lower momentum ratios as compared to low density ratio coolant jets. However, the physics of jet-mainstream interaction is essentially the same. It is easier to use ambient air as a coolant for experiments and testing with a density ratio of 1.0 is therefore popular. Assuming that the surface is adiabatic, a film cooling effectiveness, $\eta$, is defined as

$$\eta = \frac{T_\infty - T_{aw}}{T_\infty - T_c} \tag{1}$$

Here, $T_{aw}$ is the adiabatic wall temperature downstream of injection. $T_\infty$ is the freestream temperature. For low speed flows, recovery temperature, $T_{rec}$ can be used instead of freestream temperature. This is useful for finding the effectiveness using an optical method such as infrared thermography. $T_c$ is the coolant exit temperature. Film effectiveness $\eta$, is a nondimensional measure of the surface temperature downstream of injection with maximum value of 1.0 for $T_{aw} = T_c$ and minimum value of 0.0 for $T_{aw} = T_\infty$. The use of a plenum to feed the coolant tubes results invariably in conduction effects through the plate. If the coolant is supplied through tubes this conduction effect is almost nonexistent except in the immediate proximity of the hole. A good review of parametric effects on film cooling is provided by Bogard et al. (Ref. 1) so only a few relevant studies are cited in this review to provide the reader with some background to the work reported in this paper.

A popular dataset used for CFD validation is that of Sinha et al. (Ref. 2). They report span averaged and centerline adiabatic film cooling effectiveness on a flat plate with a row of 7 cooling holes inclined at 35° for density ratios of 1.2, 1.6, and 2.0. The blowing ratios varied from 0.25 to 1.0. The data was taken using surface mounted thin ribbon thermocouples at several spanwise and axial locations. The cooling holes were spaced 3 diameters apart and were fed from a plenum in a direction normal to the flat plate. The L/D for the study was 1.75. The test plate used Styrofoam with a conductivity of 0.027 W/m$^2$K. For a density ratio of 1.2, a 50 K temperature difference between free stream and coolant was used. Uncertainty in temperature is reported to be 0.1 K.

The short hole lengths contribute to jet detachment at lower blowing ratios. A comparison with the data of Pederson et al. (Ref. 3) shows this trend for all but the lowest blowing ratio. Pederson et al. used long holes inclined at 35° to study the effect of density ratio on effectiveness. They used a mass transfer technique over a wide range of density and momentum ratios.

Bons et al. (Ref. 4) performed experiments to study the impact of free stream turbulence on film cooling effectiveness downstream of discrete cooling holes injecting coolant into the freestream at an angle of 35° from the surface and in the downstream direction. Turbulence intensities from 0.9 to
17 percent were studied. Flow uniformity of 2.5 percent was achieved with free stream velocity of 16 m/s. Blowing ratios of 0.55 to 1.5 are reported. The density ratio for the study was 0.95. Surface temperature was measured using

thermocouples under an Inconel foil that is not heated so that the wall is adiabatic. They found that at low blowing ratios, high turbulence intensity led to deterioration of cooling effectiveness while at high blowing ratio, high free stream turbulence improves laterally averaged effectiveness. This is consistent with what one would expect because high turbulence enhances mixing which is useful if the jet is detached but is a source of loss (leading to higher temperature at surface) if the jet is attached and already providing film cooling coverage. These results are supported by a study by Mayhew et al. (Ref. 5) who used Liquid Crystal Thermography to study adiabatic film cooling effectiveness for a configuration similar to that of Bons et al. at various blowing ratios.

Lutum et al. (Ref. 6) studied the effect of length to diameter ratio on film cooling effectiveness for a 35° injection hole and blowing ratios from 0.52 to 1.56. They found that the effectiveness increased with the length to diameter ratio although the variation is small in the range of $5<L/D<18$. It is possible however that this result is dependent on plenum boundary conditions which were not taken into account. Thermochromic liquid crystal was used in conjunction with thermocouples to determine the adiabatic effectiveness.

Surface roughness effects can be a major influence on film effectiveness via its role in changing the heat transfer coefficient. At engine scale, roughness of several hundred microns can be on the order of magnitude of the hole diameter. Modeling roughness is then an added complexity for CFD. The effects of roughness are very similar to those of free stream turbulence in that increased roughness can be beneficial at high blowing ratios while it is detrimental at lower blowing ratios.

One of the consistent problems with the aforementioned experiments is that they required invasive techniques to determine the adiabatic effectiveness. A benchmark data set for film cooling should allow the computational modeling effort to focus on solving the mixing problem in the near-hole region without having to introduce conjugate heat transfer. Infrared thermography is a non-invasive technique thereby allowing CFD to model the experiment more closely. There is also a lack of uncertainty analysis related to laterally averaged film effectiveness. To eliminate the effect of the plenum on heat transfer and flow physics in the hole, it is desirable to use long holes without a plenum.

Thurman et al. (Ref. 7) presented results from a study that used long holes ($L/D\sim15$) for blowing ratios of 1 and 1.9. The basis for the use of long tubes for the coolant holes was to yield a well-developed velocity profile at the hole exit. Span-averaged effectiveness values were not reported in the study of Thurman et al. and the focus was to qualitatively compare an anti-vortex hole geometry to a round hole geometry. Nusselt number distributions on the surface were shown using a Liquid Crystal technique.

Han et al. (Ref. 8) provide a review of measurement techniques used in studying film cooling. These range from surface mounted thermocouples for surface temperature measurements to Particle Image Velocimetry for full field flow visualization. Infrared cameras have now been used with some regularity for qualitative thermal imaging and for non-destructive evaluation of engine components. Infrared cameras measure radiation not just from the object being viewed but also radiation reflected by the object and emanating from other environmental sources in the vicinity. There is also a loss of radiation due to atmospheric absorption or due to the optical properties of the viewing window. These properties change with time and must therefore be accounted for during each measurement to obtain accurate temperatures. This requires the use of multiple reference temperatures. The parameters that influence the temperature measurement are emissivity of the object surface, the reflected apparent temperature, the distance between the object and the camera and the ambient or background temperature. Over short distances, the atmospheric transmission losses (influenced by relative humidity) are small enough to be neglected. However, the use of an optical window introduces another loss mechanism that must be accounted for.

As early as 1979, Papell et al. (Ref. 9) used infrared images to study the variation in film cooling effectiveness due to the curvature of the coolant tubes. Blowing ratios of 0.37 to 1.25 were tested using a temperature difference of 25 K between coolant and tunnel inlet. Baldauf et al. (Ref. 10) used infrared images to show surface effectiveness on a flat plate with thermal conductivity of 0.3 $W/m^2K$. The hole length was six times the diameter and pitch to diameter ratios of 2, 3, and 5 were tested. Density ratios of 1.2, 1.5, and 1.8 were reported. Ekkad et al. (Ref. 11) used a transient infrared thermography technique to determine simultaneously the surface effectiveness and heat transfer coefficients for a single hole on a half cylinder using a FLIR SC3000 camera. They used a reference thermocouple to measure the surface temperature without flow. The emissivity of the surface was varied to obtain a temperature on the infrared camera that matched the thermocouple temperature.

Wright et al. (Ref. 12) used pressure sensitive paint to obtain surface effectiveness distributions at a density ratio of 1.4. Blowing ratios were varied between 0.25 to 2.0 for free stream turbulence intensities between 1 to 12.5 percent for cylindrical and fan shaped holes inclined at 35° and spaced 4 hole diameters apart.

The present study includes detailed measurements of turbulence, velocity and temperature (presented in this report) using thermocouple surveys and infrared thermography for two different nominal free stream turbulence intensities: 1.5 percent, referred to as ‘low *Tu*’ and 8 percent, referred to as ‘high *Tu*’ or ‘with turbulence grid’. The

turbulent intensity at the CFD inlet plane location is estimated to be 2 percent for the 'low *Tu*' case and 14 percent for the 'high *Tu*' case. Air that was chilled by passing it through an ice bath was used as coolant. The coolant was introduced into the main stream through long tubes (L/D>18). Both span averaged and centerline effectiveness are reported. Infrared thermography allows for full field thermal mapping of the test section.

For film-cooling flows in the higher blowing ratio range, (0.8 to 2.0), Reynolds Averaged Navier Stokes (RANS) simulations do not produce accurate solutions (Refs. 13 and 14). Argument is made that RANS models are not adequate for film-cooling flows because they involve unsteady interactions and large-scale mixing of the main stream and cooling stream. This needs to be better accounted for by direct modeling of these interactions. In recent years, attempts have been made to model film cooling flows using Large Eddy Simulation (LES) and Detached Eddy Simulation (DES). Some of these attempts have resulted in computations of cooling effectiveness while others have used LES to shed light on the physics of film cooling. Guo et al. (Ref. 15) studied blowing ratios of 0.1 and 0.48 for normal and 30° inclined angles using LES. Their purpose was to investigate the turbulent flow structure and the vortex dynamics for gas turbine blade film cooling. Their work showed that the turbulent flow downstream of the hole is highly anisotropic and that LES is well suited for such simulations. Tyagi and Acharya (Ref. 16) studied film cooling physics for a blowing ratio of 0.5. They showed good agreement with experiment for velocity distributions downstream of the hole and shed light on the physical features of the film cooling flow such as the resolution of hairpin vortices downstream of the holes. More recently, Fujimoto (Ref. 17) used surface-adjusted octree hexahedral meshes to perform LES computations of film cooling effectiveness. He showed a comparison of his results and the results of a multi-block LES computation with the experimental data of Sinha et al. (Ref. 2). He reported good agreement with the experimental data for a range of blowing ratios.

One of the issues often confronted when computing film-cooling flows is the effect of the plenum. Modeling the plenum and the assumptions concerning such modeling is a source of uncertainty. Including the plenum in the numerical model is often done but the incompressible flow within the plenum reduces the convergence rate of the numerical schemes. This limitation has little to do with the actual engine conditions and is encountered because experimental setups use plena for film cooling. To realistically model the flow the plena have to be included in the computations. Earlier works in LES for film-cooling flows includes the work of Peet and Lele (Ref. 18) who used a combination of CFD codes namely an incompressible method for the plenum and the pipe and a compressible code for the cross-stream and the interaction zone. They computed turbulence statistics and effectiveness of the film-cooling for a low, blowing ratio case of $M = 0.5$.

In the present study a Time-Filtered Navier-Stokes (TFNS) method is used to compare film cooling effectiveness computations of long-hole film cooling to infrared thermography and thermocouple surveys. This method is also referred to as Partially Resolved Navier Stokes or PRNS and the two terms (TFNS and PRNS) are used interchangeably. Flow over a flat plate and temperature distribution downstream of film cooling holes at a 30° inclination at blowing ratios of 0.5, 1.0, 1.5, and 2.0 for a single nominal density ratio of unity were simulated. The range of momentum ratios is thus the same as the blowing ratios. Some earlier computations (Refs. 13 and 14) performed at the blowing ratio of $M = 2$, showed the inadequacy of the $k$-$\omega$ turbulence model (Ref. 19) at high blowing ratios. In this study, several turbulence models within the Glenn-HT code (Ref. 20) were used for an intermediate blowing ratio of unity. In addition, a commercial code, CFX and the models within it (SST and k-$\varepsilon$) were also applied and it was verified that high blowing ratio cases were not well reproduced. Near-hole results were especially of concern as the discrepancy between the predictions and data was large enough to require reconsideration of the method of data-acquisition in that locality.

The unsteady approach called the Time-Filtered Navier-Stokes (TFNS), (also referred to as Partially Resolved Navier-Stokes (PRNS) or Very Large Eddy Simulation in earlier papers by the developer team at NASA) (Refs. 21 and 24), was developed at NASA Glenn Research Center. The method was developed for the simulation of large turbulent eddies requiring grid resolution comparable to what is often used in RANS simulations. The method is based on the concept of temporal filtering. This avoids issues associated with coarse grids that directly influence the solutions in LES due to the filter size being directly connected to the grid resolution. In TFNS, the larger time scales (or lower frequencies) of the turbulence are directly calculated and the effects of the unresolved time scales of the turbulence are modeled by a dynamic equation system. The contents of both the resolved and unresolved turbulence are regulated by a "Filtering Control Parameter" (FCP), which is related to the width of the temporal filter.

The basic equations of TFNS and its subscale model, as presented by Shih and Liu (Ref. 23) are grid invariant, i.e., they do not have grid spacing as a parameter in their formal formulations. Therefore, it is possible to achieve a grid-independent numerical solution. Shih and Liu (Ref. 23) count this as a major point of departure from the traditional LES approach and its variants. Another distinction is that TFNS enables performance of unsteady RANS (URANS), LES, and even DNS in a unified way through the judicious selection of the value of FCP, and the

appropriately refined grid. It should be noted that the TFNS approach is not a variant of the popular hybrid RANS/LES (e.g., Refs. 25 to 28). There is no enforced transition between the perceived RANS and LES domains.

The subfilter model is constructed to use a more general relationship between the unresolved turbulent stresses and the resolved turbulent flow field, Shih and Liu followed the analysis of the rational mechanics and obtained a general constitutive relationship for the Reynolds stresses following (Ref. 23). The constitutive relationship in addition to an eddy-viscosity term includes several other terms representing the anisotropy and the rotation effects due to the interactions between the resolved and unresolved turbulence. In addition to the dissipative and diffusive effects accounted for through the eddy viscosity, the effects of anisotropy and rotation are accounted for in the subscale model, when the simulation pertains to the very large eddy simulation. Source terms introduced in the momentum equation sustain the turbulent fluctuations in the calculated flow field. One important outcome of the use of this constitutive relationship is the ability of the TFNS to sustain turbulent fluctuations for a turbulent pipe flow in the lower range of applicable Reynolds numbers. The k-ε variant was not able to sustain a turbulent flow physically. The model adopted for the TFNS simulations in the Glenn-HT code employs this unique feature of the nonlinear subscale model.

## III. Setup of Experiment

A thirty times engine scale test facility was used to interrogate the complex, highly three-dimensional flow field associated with detached flows and to specifically resolve the shear layers and wake regions. A schematic of the flow and geometry for the test are shown in Figure 1. Experiments were carried out in the wind tunnel shown in Figures 2, 3 and 4. This is an open loop tunnel with a temperature controlled coolant loop. The tunnel consists of an aluminum bellmouth, flow conditioning screens, square acrylic sections that are 0.208 m wide and 0.0191 m thick, the test section on the floor of the tunnel and a lid directly above it for either viewing or actuator support. Air was drawn from the room and passed through flow conditioning sections prior to entering the test section.

Airflow was provided by a 5220W fan. The freestream velocity was 9.1 m/s and the Reynolds number based on freestream velocity and coolant hole diameter was 11,000. The test section is a square section of cross section measuring 0.2083 by 0.2083 and 0.8636 m in length. The freestream turbulence intensity measured approximately 1.5 percent without a grid and 8 percent with a square grid based on hotwire surveys. The boundary layer thickness at x/d = –0.5 is 0.0127 m and is taken to be the vertical distance from the wall at which the velocity is equal to 99 percent of the freestream velocity.

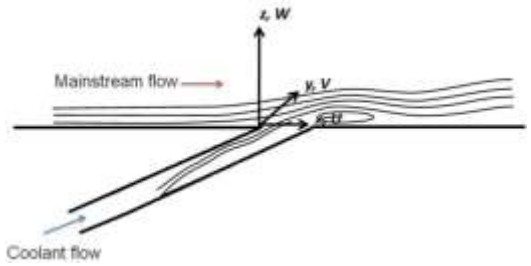


Figure 1.—Schematic of cooling flow.

Figure 2.—SW-6 low speed wind tunnel.

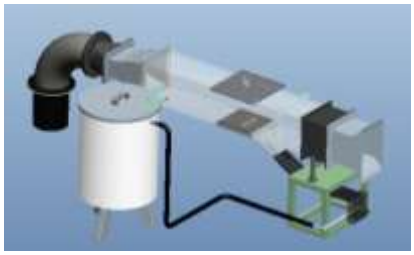

Figure 3.—CAD model of SW-6 facility.

The coolant flow was provided by blowing pressurized supply air through a heat exchanger, which consisted of a copper tube coiled inside an ice–water tank. The coolant was then fed through a manifold to three separate flow meters, and then to acrylic tubes with L/D = 20 connected to each cooling hole. The separate cooling tubes provided an opportunity to model the cooling flow in each hole as fully developed.

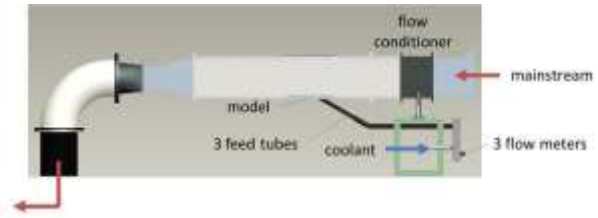


Figure 4.—Schematic of test setup.

Figure 5.—Film cooling test plate with long holes.

The test section (Figure 5) was a flat plate made of acrylic with three holes inclined at 30° and a hole diameter of 0.019 m. The hole spacing was y/d = 3. To determine the tunnel flow rate, a total pressure probe was placed upstream of the test section and static pressure taps were placed on the sidewalls. Freestream temperature was measured with an open-ball thermocouple located upstream of the holes near the total pressure probe. Coolant temperature was measured with open-ball thermocouples inside the coolant tubes. Temperature survey data was taken along the centerline plane of the tunnel and at several cross sectional planes with a small, open ball, type E thermocouple probe attached to an actuator above the test section. The adiabatic wall temperature was determined from the thermocouple probe surveys with the probe located near the floor of the test section. Various hotwire probes (Ref. 7) were used to obtain the three-dimensional velocity components and turbulent stresses along the centerline and at several streamwise planes.

## Description of IR Measurement Setup

To obtain the adiabatic film cooling effectiveness a FLIR SC655 infrared camera was used with multiple temperature ranges. For the work reported the range of –293.15 to 423.15 K was used. This corresponds to a wavelength of approximately 10 μ. A ZnSe window was used with a transmittance of 0.96 in the 9 to 11 μ range. The resolution was approximately 81 pixels/in. or 3.2 pixels/mm. This corresponds to 108 pixels/D. The specified accuracy of the camera is 2 percent of the measured temperature. The temperature range being examined is approximately between 285 and 300 K corresponding to an object signal range of 117 to 137. The maximum error due to neglecting reflection and background corrections is 1.49 percent of object signal or ±1 K.

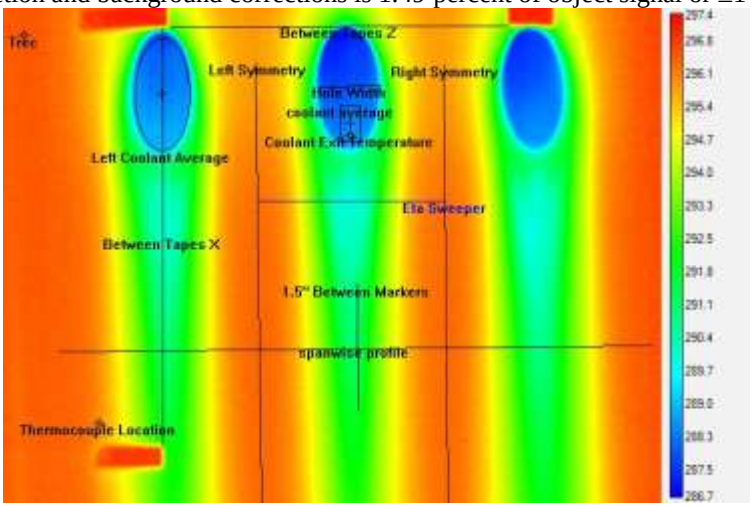


Figure 6.—Infrared thermograph showing regions of interest.

Film cooling effectiveness is calculated as

$$\eta_{\text{method1}} = \frac{T_{\text{rec}} - T_{aw}}{T_{\text{rec}} - T_c} \tag{5}$$

where each value on the right hand side of the equation is a surface measurement from a single IR image. Figure 6 shows an example of an IR image with regions of interest marked for reference.

The thermocouple location for reference measurements is marked in the lower left corner as 'Thermocouple Location'. The recovery temperature, $T_{rec}$, is measured using a 9-pixel average at the upper left location marked 'Trec'. This marker is located at a spanwise distance of 0.75 p/d from the left coolant hole leading edge. Coolant temperatures are measured using three different regions of interest. An elliptical region consisting of 4598 pixels, labeled 'Left Coolant Average', is used to measure average coolant temperature over the visible portion of the left hole wall. A 9-pixel marker labeled 'Coolant Exit Temperature' measures the exit temperature on the wall of the center cooling hole nearest to the cooling hole exit. It is located at a distance of *1.7 D* upstream of the hole trailing edge and along the centerline. This corresponds to a location of y/d = –0.1 at which the coolant temperature from CFD is extracted.

A rectangular averaging marker labeled 'coolant average' measures coolant exit temperature over 612 pixels. The temperatures measured by these three different markers are within 0.1 K. For effectiveness, the temperature measured by the 'Coolant Exit Temperature' marker is used to match results from CFD. The line marker 'eta sweeper' is used to sweep the surface between the left and right symmetry markers shown in Figure 6 between x/d = 0 and x/d = 6.0. The marker width is equal to 1 pitch. The skewness of the image is compensated for in the calculations. The error in location coordinates arises from converting pixels to physical units. In this case, the primary reference for measurement is two marker points spaced 0.0381 m (1.5 in.) apart and shown in Figure 6 as '1.5 in. Between Markers'. In addition, the distance between two pairs of metal tapes is also known with the distance specified by 'Between Tapes X' being 0.127 m (5 in.) and 'Between Tapes Z' being 10.4775 m. The corresponding pixel locations are used to determine the ratio of pixels to physical length. The hole diameter is then ascertained based on this conversion and is found to be accurate to 0.5 pixels or 0.0001524 m for all cases. These calculations are all performed using an image exported from the infrared camera and processed by in-house written MATLAB (The Mathworks, Inc., Natick, MA) routines. It is evident that as the dimension of the hole shrinks, the uncertainty of measurement location as a function of hole diameter will increase.

If it is assumed that the viewing area is small enough that the reflected apparent temperature does not vary significantly over it and that the surface emissivity and optical transmittance are uniform, the camera's total output temperature can be used instead of the true object temperature. This allows for rapid effectiveness calculations without the need to adjust reflected temperature settings during each measurement. The uncertainty introduced to effectiveness is less than ±0.002 based on an emissivity range of 0.9 to 0.98 and a transmittance range of 0.95 to 0.975. Reflected apparent temperature may vary between 273.15 and 295 K. The actual uncertainty is much smaller because the reflected temperature is much closer to the ambient temperature. For the effectiveness calculated using method 1, the reflected temperature was set to ambient temperature. The emissivity was set to 0.95 and the transmittance to 0.96 based on the material data sheet for the ZnSe window that was used. The uncertainty for the effectiveness values reported here is ±0.002 based on the definition of effectiveness used.

The effectiveness can also be calculated as, $\eta_{\text{method2}} = \frac{T_\infty - T_{aw}}{T_\infty - T_c}$. Here, the tunnel inlet temperature, $T_\infty$, is used instead of the recovery temperature. This temperature is obtained using the type *E* thermocouples described in the previous section. The coolant temperature is also obtained using thermocouples. In this case, the emissivity and reflected temperature are varied until the temperature measured by the IR camera at the reference thermocouple location is within ±0.05 °C of the temperature indicated by the reference thermocouple and the coolant exit temperature matches the thermocouple measured coolant temperature within ±0.05 °C. The uncertainty in transmission is ±0.01.

## IV. Setup of Numerical Domain

Film cooling flow computations were undertaken using the NASA Glenn-HT (Ref. 13) code. The code is a multi-block structured-grid N-S solver. The computational domain extended 12 cooling hole diameters upstream of the cooling hole and 16 diameters downstream. Spacing between the holes in the experiment was equal to three hole-diameters and there were three holes. For the computations a period of 3 diameters was imposed. It was however understood that due to flow unsteadiness, imposition of periodicity is a simplification that is done for the

sake of reducing resource requirements for the computations. The free-stream was placed at 5 diameters from the wall. A number of grid blocks were assigned to individual CPUs in a balanced manner to allow parallel computing. To reduce the communications overhead, smaller blocks were further consolidated before the grouping was implemented. For the present computations, initially 120 groups (CPUs) were used but by refining the blocking, it was possible to increase the number of CPUs to 1200 for better parallel capability. The grid itself contained approximately 8 million cells. Particular attention was paid to refinement of the grid in areas near the no-slip walls and near the cooling hole outlet and especially downstream of the cooling hole. The grid cells in the core of the film cooling flow were constructed to be uniform and near cubic. The overall grid topology, the symmetry plane of the computational domain, as well the near-hole grid shown from two views are presented in Figures 7(a) and (b).

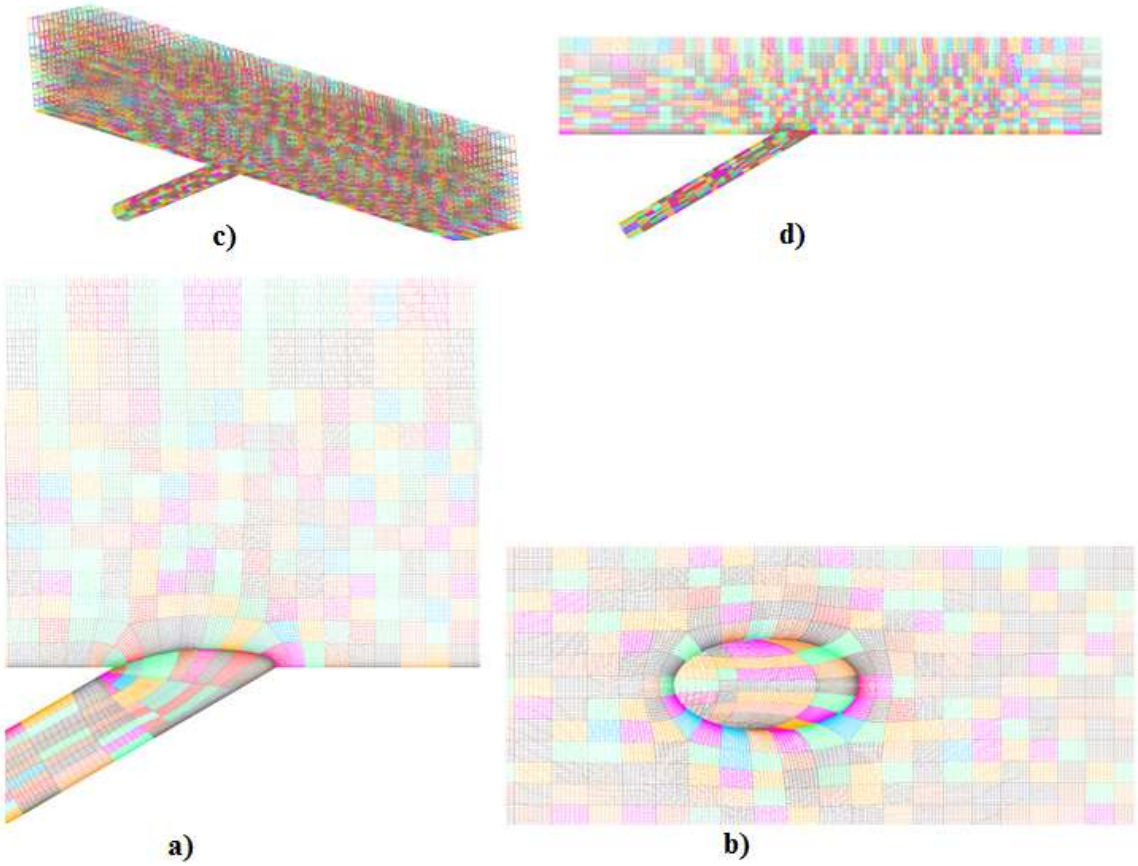


Figure 7.—Computational grid showing views of the grid near the hole exit (a) and (b), the computational domain (c) and the grid blocking for parallel computing (d).

The simulations were conducted according to the conditions provided by the experiments. Geometric scaling was performed to raise the flow Mach number while maintaining the Reynolds number based on the film cooling hole. The density ratio of the flow was held to near unity by adjusting the total temperature at the hole inlet. Blowing ratios of 0.5, 1.0, 1.5, and 2.0 were computed. The cases were run primarily using the TFNS model with the Filtering Control Parameter, $\left(\frac{\Delta_T}{T}\right) = 0.16$ which produced a factor of $f_i = 0.3$ (Ref. 23).

As mentioned earlier, experience suggests that the film cooling effectiveness cannot be predicted with RANS when the blowing ratio is relatively high (>~1). The computations at high blowing ratios presented here, attempt to model the film cooling flow with a TFNS model to verify that a better film cooling effectiveness prediction may be obtained.

## V. Results and Discussion

In this section results from CFD, thermocouple surveys and infrared thermography are shown for blowing ratios of 0.5, 1.0, 1.5 and 2.0. For blowing ratio of 2.5 only infrared thermography data is presented. The results are divided into sections based on nominal blowing ratio. For the 1.0 and 2.0 blowing ratios, results from hotwire anemometry are also presented in terms of Nondimensional velocity, turbulence intensity, shear stress and length scale.

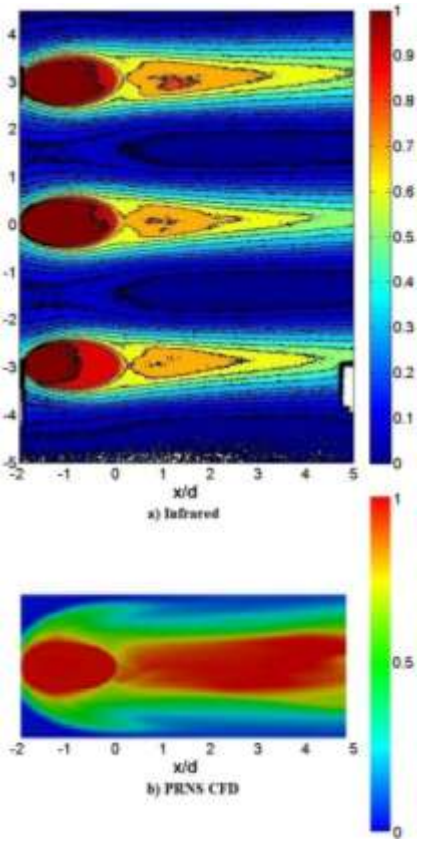


Figure 8.—Film cooling effectiveness from (a) infrared thermography and (b) CFD for M = 0.5, DR = 1.0, Tu = 1.5 percent.

### Blowing Ratio = 0.5

Figure 8 shows the surface effectiveness values computed according to method 1 described in the previous section as measured by the infrared camera. The values range from 0 (indicating no cooling) to 1.0 (indicating the coolant temperature or maximum effectiveness.) For this case the image shows some asymmetry in the surface temperature downstream of the holes located at y/d = 3 and y/d = –3. The flow exiting the central hole is very similar to that exiting the hole at y/d = 3. It is possible that the flow exiting the hole at y/d = –3 is warmer due to an imperfect seal formed by the thermocouple in the coolant tube. The region of interest however is downstream of the central hole located at y/d = 0.0 so the variation in temperature exiting the adjacent hole is a second order effect. There is a necking of the surface coverage immediately downstream of the hole followed by a rise in effectiveness further downstream up to x/d = 1 followed by a steady drop in effectiveness. The region between y/d = 1 and y/d = 2 sees little cooling downstream of the hole. The near hole region however appears to be cooled through the action of the horseshoe vortex and mixing of the coolant with the freestream. The contours in the cooling hole do not show a uniform effectiveness of 1.0 over the area of the hole because the IR camera shows the temperature on the surface of the coolant tube as a projection. A key point to note therefore is that the coolant exit temperature indicated by the IR camera is different from the temperature measured by the thermocouples in the coolant tube.

The temperature rise from coolant measurement location to hole exit would shift effectiveness measured using thermocouples by up to 0.04 higher. However, it is impractical to place a thermocouple however small at the coolant hole exit due to its influence on the jet. It is important therefore to treat the thermocouple measurements independently of the infrared measurements when comparing to future or existing datasets. Figure 9 shows effectiveness measured by thermocouple surveys and processed using Tecplot. In Figure 9, planes at x/d locations 0.133, 2.133, 4.133, and 6.133 downstream of the cooling hole are shown along with a plane at the centerline. Flow is from left to right along the x/d axis. The contours show the coolant core sticking close to the surface and gradually dissipating while providing a wide area of cooling.

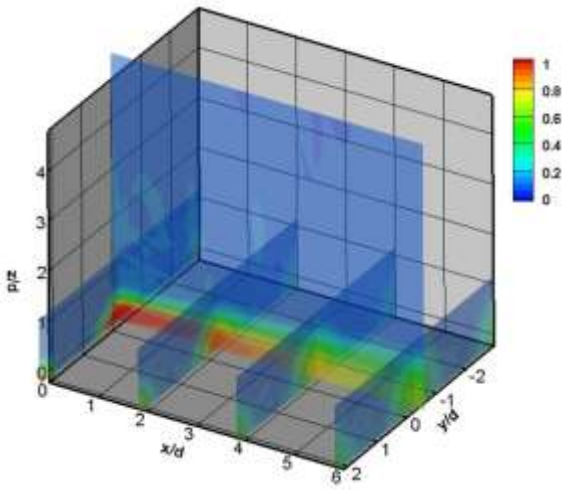


Figure 9.—Film effectiveness from thermocouple surveys for M = 0.5, DR = 1.0, Tu = 1.5 percent.

Figure 10 shows iso-surfaces of the Q-criterion (Ref. 29) which represents locations in the flow where the rotation dominates the strain and shear. The cooling fluid with the higher density is shown to propagate downstream with periodic mixing patterns appearing first at a location slightly upstream of the hole and staying regular some distance downstream before it becomes more random. Q-criterion serves to highlight vortical structures within the turbulent flow. The patterns indicate definite ring vortices that are formed around the film column and convect downstream. These rings are quite regular and appear to be of the Kelvin-Helmholtz instability type. Further downstream of the hole the patterns appear to have dissipated due to turbulent mixing. The surfaces are colored by non-dimensional temperature, $\theta = 1-\eta$. Thus, the blue regions show cooling flow while the red regions are at freestream conditions. The coherent vortical structures persist for several hole diameters downstream of the hole and then break up. This coincides with the rapid deterioration in effectiveness seen in Figure 8 especially in the spanwise direction (seen by sharp narrowing of the color bands.) This is akin to waves breaking up and churning up the ocean below. It is possible that the prediction of the breakup of these vortices could be the key to accurate prediction of film cooling effectiveness far downstream of the hole.

Figure 11 shows film effectiveness at the jet centerline (y/d = 0) from thermocouple surveys. A curvature of the coolant jet is seen at x/d = 1 that is coincident with the rise in effectiveness observed in Figure 8 at the same location. This indicates the migration of the jet core toward the surface due to the influence of the freestream. The influence of the jet extends to z/d = 0.3 at the hole trailing edge and to
z/d = 1.1 at x/d = 5.25.

Figure 12 shows contours of effectiveness at x/d = 0.133 (top), 2.133, 4.133, and 6.133 (bottom) downstream of the cooling hole. The spanwise extent (y/d) of the figures is 1 pitch (3 hole diameters.) The core is seen to stick close to the surface and the jet spreads out gradually as it mixes with the freestream. The effectiveness of the core drops from 1.0 at the hole exit to 0.7 at x/d = 6.133. The cooling jet spreads gradually downstream of the hole in agreement with the IR image form Figure 8. The vertical extent grows from 0.7 to 1.3 y/d from x/d = 0.133 to x/d = 6.133. The coldest region of the jet also changes from elliptical with a spanwise major axis to elliptical with major axis in the vertical direction.

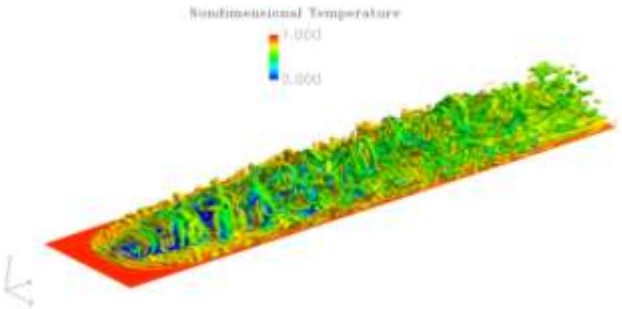


Figure 10.—Q-criterion showing Kelvin-Helmholtz instability at M = 0.5, DR = 1.0, Tu = 1.5 percent.

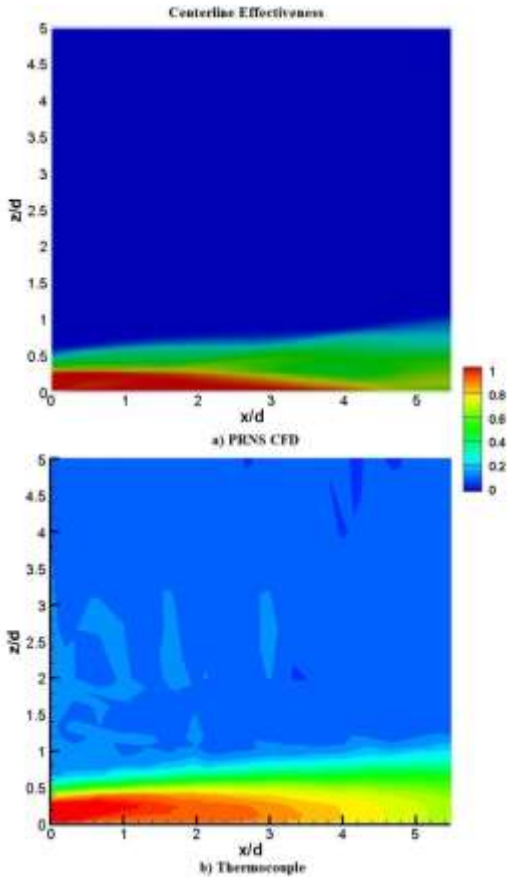


Figure 11.—Centerline effectiveness from (a) CFD, (b) thermocouple at M = 0.5, DR = 1.0, Tu = 1.5 percent.

Figures 13 and 14 show span-averaged and centerline effectiveness for M = 0.5, respectively. The cyan line shows effectiveness from IR thermography for the high *Tu* case (8 percent). The results from IR thermography for low turbulence lie within the error bands of the thermocouple data for low turbulence. The black dashed lines bound the results from IR measurements with the red dashed line representing an IR measurement that has been calibrated using a surface mounted thermocouple and a thermocouple in the coolant tube.

This proves that at the small temperature ranges in use for this experiment, as long as effectiveness is computed using values from a single image, no significant error or penalty is incurred. However the same assumption does not extend to larger temperature differences that would require careful calibration using several surface mounted thermocouples at a range of temperatures that include the coolant and free stream temperature.

It is interesting to note that the CFD results show a relatively high effectiveness maintained much further downstream of hole than the experiment. The IR results shown in Figure 14, show that higher turbulence intensity is

initially beneficial to mixing the jet at the hole exit but then causes a deterioration in centerline effectiveness downstream as the near-surface coolant is forced to mix with the freestream more rapidly and spread out. The span-averaged effectiveness however is higher for the case of high turbulence. This is consistent with the results of Brown et al. (Ref. 30) who found that above a blowing ratio of 0.7 higher turbulence intensity caused higher span averaged effectiveness but reduced centerline effectiveness. Figure 8 shows a 'necking' of the effectiveness contours downstream of the hole and this is indicative of the lift-off tendency of the jet. At higher density ratio, this lift-off would occur at a lower blowing ratio due to the increased momentum of the jet. Figure 12 shows that CFD predicts the Kelvin-Helmholtz structures persist to approximately x/d = 4 at which point they begin to break up. It would suggest that this coherence is the cause of the relatively high effectiveness shown by CFD for low blowing ratios. At higher blowing ratios, it is conceivable that this same effect would have deleterious consequences. Downstream of the breakup region, the TFNS model, causes a rapid mixing of the jet and freestream resulting in an increased rate of decline of effectiveness.

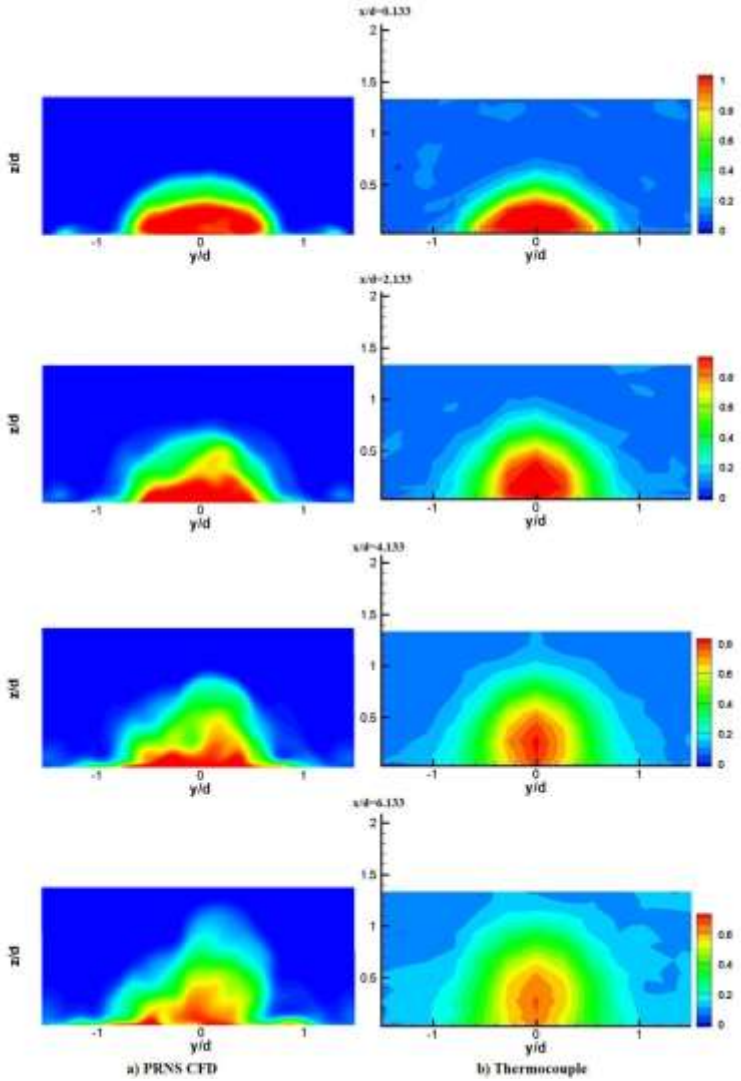


Figure 12.—Effectiveness contours from (a) CFD, (b) thermocouples at planes of constant x/d for M = 0.5, DR = 1.0, Tu = 1.5 percent.

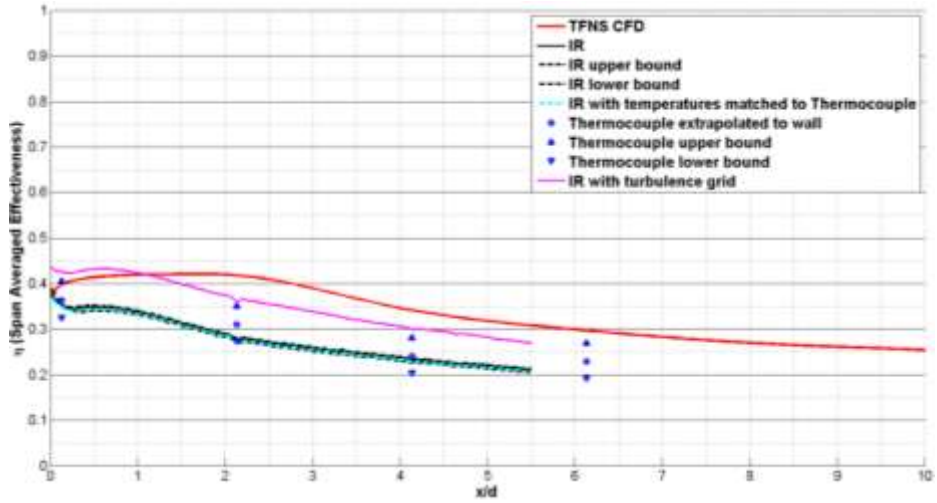


Figure 13.—Spanwise-averaged film effectiveness for M = 0.5, DR = 1.0.

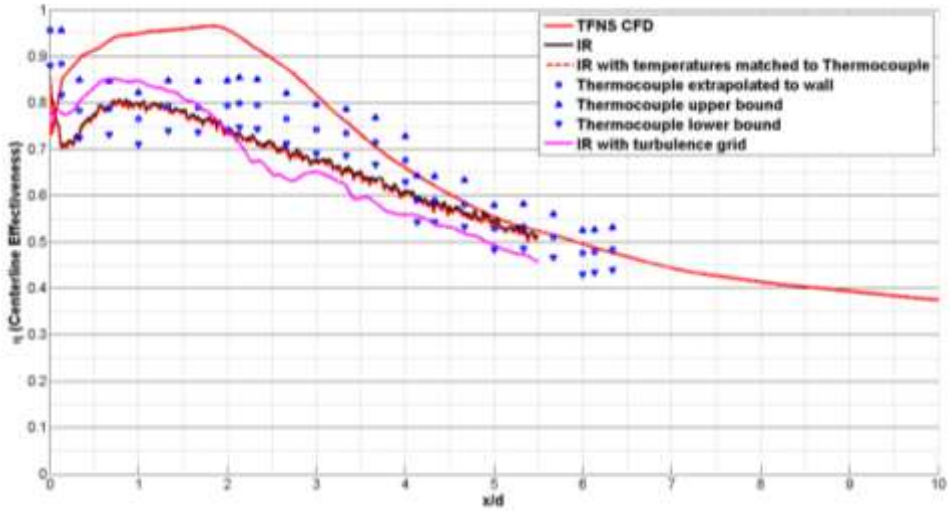


Figure 14.—Centerline film effectiveness for M = 0.5, DR = 1.0.

**Blowing Ratio = 1.0**

Figure 15 shows surface effectiveness for a blowing ratio of 1.0 from IR thermography for the low turbulence intensity case. The maximum effectiveness downstream of the hole has dropped to approximately 0.45 and occurs at approximately 2.5 diameters downstream of the hole trailing edge. In addition, the contours appear to be pinched and aligned with the flow direction. This indicates that the jet core may already be lifted away from the surface.

The contours in Figure 15 indicate that there is uniform cooling that seems to extend far downstream and doesn't drop off as quickly as for M = 0.5. The coverage appears only to extend to y/d = ± although there is a gradual spreading of the jet as it progresses downstream. There is a sharp neck at x/d = 0.5, although, it is not as pronounced as it is for M = 0.5 because the jet trajectory is now directed away from the surface. Near the hole exit where the coolant temperature is measured, the coolant is influenced by the jet mixing that causes a drop in effectiveness. The contour rings around the hole are a combined effect of the horseshoe vortex and to a lesser extent, localized conduction due to the finite thickness of the flat plate. Figure 16 shows effectiveness calculated from thermocouple surveys and confirms that the jet is in fact lifting from the surface. Planes at x/d locations of 0.133,

2.133, 4.133, and 6.133 downstream of the cooling hole are shown along with a plane at the centerline. Flow is from left to right along the x/d axis. Figure 17 (a) and (b) show turbulence intensity, *Tu* and Nondimensional velocity, $U/U_{inf}$ respectively. The jet trajectory of 17 (b) matches that shown by the thermocouple surveys in Figure 16 but is not as diffused. This is consistent with the difference between the thermal and momentum boundary layers. Figure 18 shows the local effectiveness at a plane located at y/d = 0.0 based on thermocouple surveys. The jet influence extends to approximately z/d = 1.4 at x/d = 1.5. The jet can be thought of as following a parabolic trajectory with a peak at x/d = 1 centered at y/d = 0.4. Notice the region between x/d = 0.5 to 2.0 where there appears to be a region of relatively lower effectiveness. The coherent hairpin vortices that are lifted off the surface allow the hot mainstream gas to be entrained under the jet. As the coherent structures breakup, coupled with the downward trajectory of the jet, the effectiveness increases near the surface again. This is borne out in Figure 19 (a) that shows turbulence intensity and in Figure 19 (c) that shows turbulent shear stress, u'w'. These results can be compared to those of Thurman et al. (Ref. 7.) From Figure 19 (c) it is clear that the top and bottom of the jet experience shear in opposing directions consistent with the vortex rollup that causes the kidney shaped vortices. Figure 19 (b) shows integral length scales. The flow conditioning screen has holes of dimension 0.2 inches and this is consistent with the largest length scales shown in the free stream. The cooling holes are long tubes with no screens or grids and thus the integral length scales in the jet are much smaller. Figure 19 (d) shows the jet resultant velocity. Figure 20 shows contours of effectiveness at planes of constant x/d. The kidney shape seen at x/d = 2.133 is seen to become less resolved at x/d = 4.133 as the jet loses coherence.

Figures 21 and 22 show span-averaged and centerline effectiveness for M = 1.0 at DR = 1.0. The thermocouple measurements show a consistently higher effectiveness in the near-hole region as the Kelvin-Helmholtz vortices are broken up and promote mixing. In the downstream region, the thermocouple results match well with IR. The CFD result starts out over predicting effectiveness because as seen from Figure 10, the hairpin vortices propagate far downstream before they break up. The pink line shows effectiveness with the turbulence grid installed and the trends follow the discussion in the previous section.

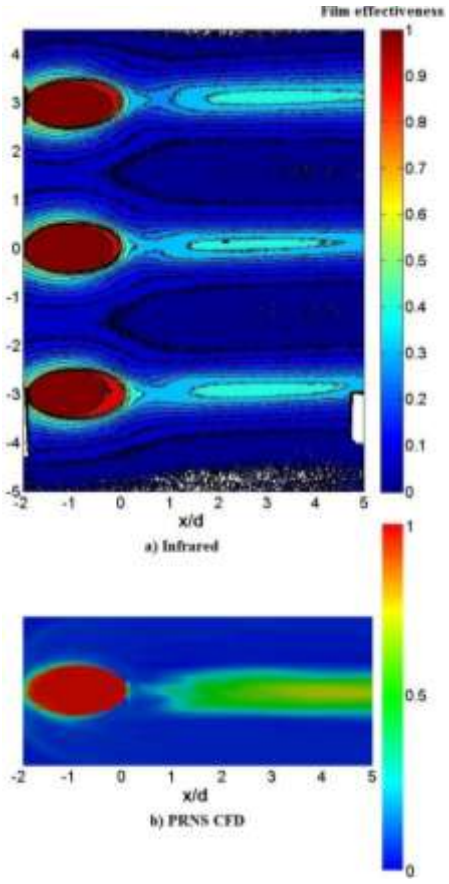


Figure 15.—Film cooling effectiveness computed from (a) infrared thermography and (b) CFD for M = 1.0, DR = 1.0, Tu = 1.5 percent.

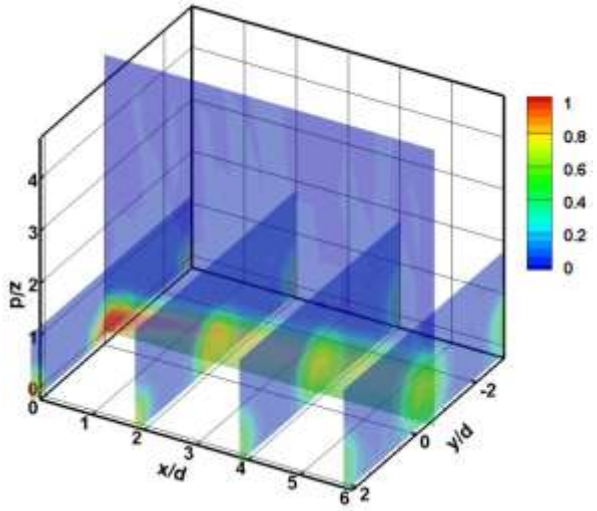


Figure 16.—Film effectiveness from thermocouple surveys for M = 1.0, DR = 1.0, Tu = 1.5 percent.

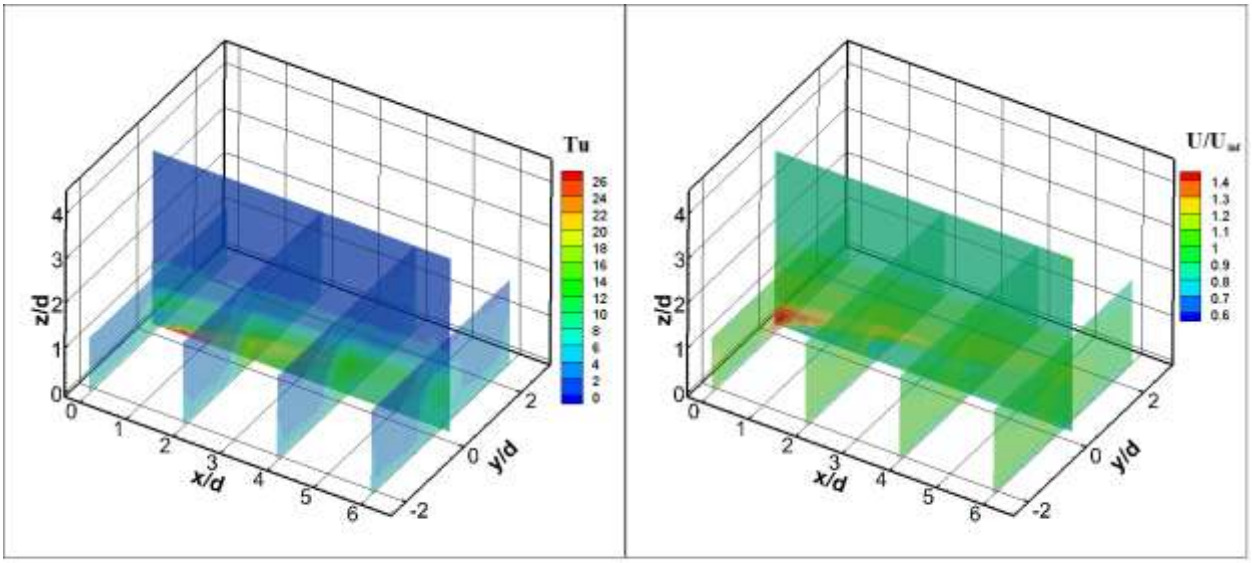


Figure 17 (a) Turbulence intesity, Tu, and (b) nondimensional velocity magnitude, $U/U_{inf}$ for M = 1.0, DR = 1.0, Tu = 1.5 percent.

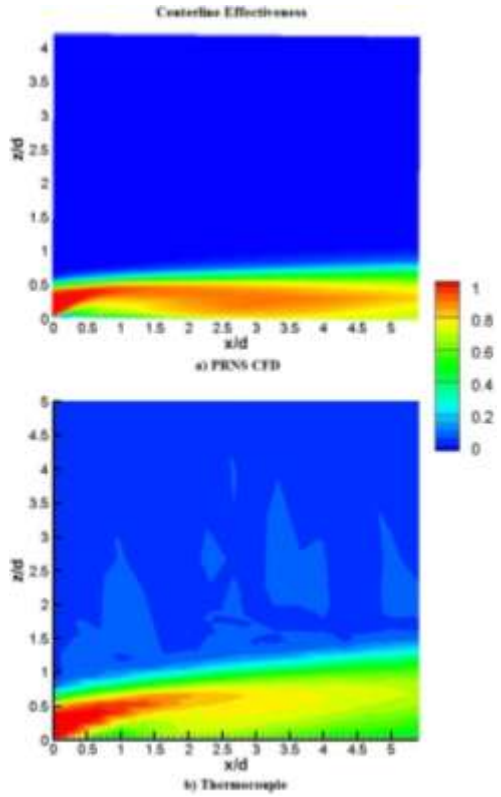


Figure 18.—Centerline effectiveness from (a) CFD, (b) thermocouple survey at M = 1.0, DR = 1.0, Tu = 1.5 percent.

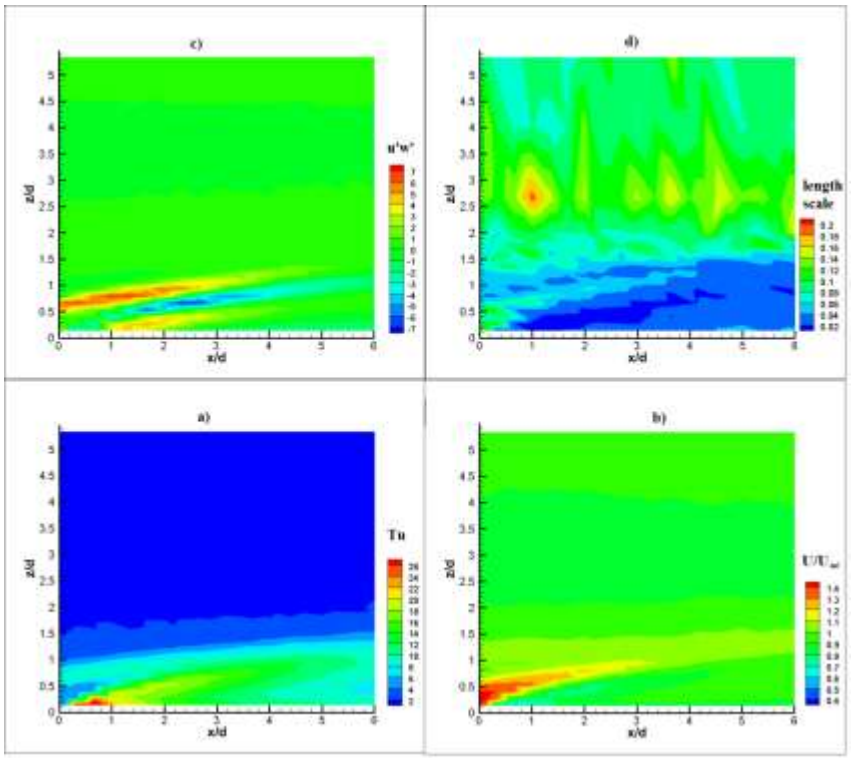


Figure 19.—Centerline contours of (a) turbulence intensity, (b) Nondimensional velocity, (c) turbulent shear stress, (d) integral length scale at M = 1.0, DR = 1.0, Tu = 1.5 percent.

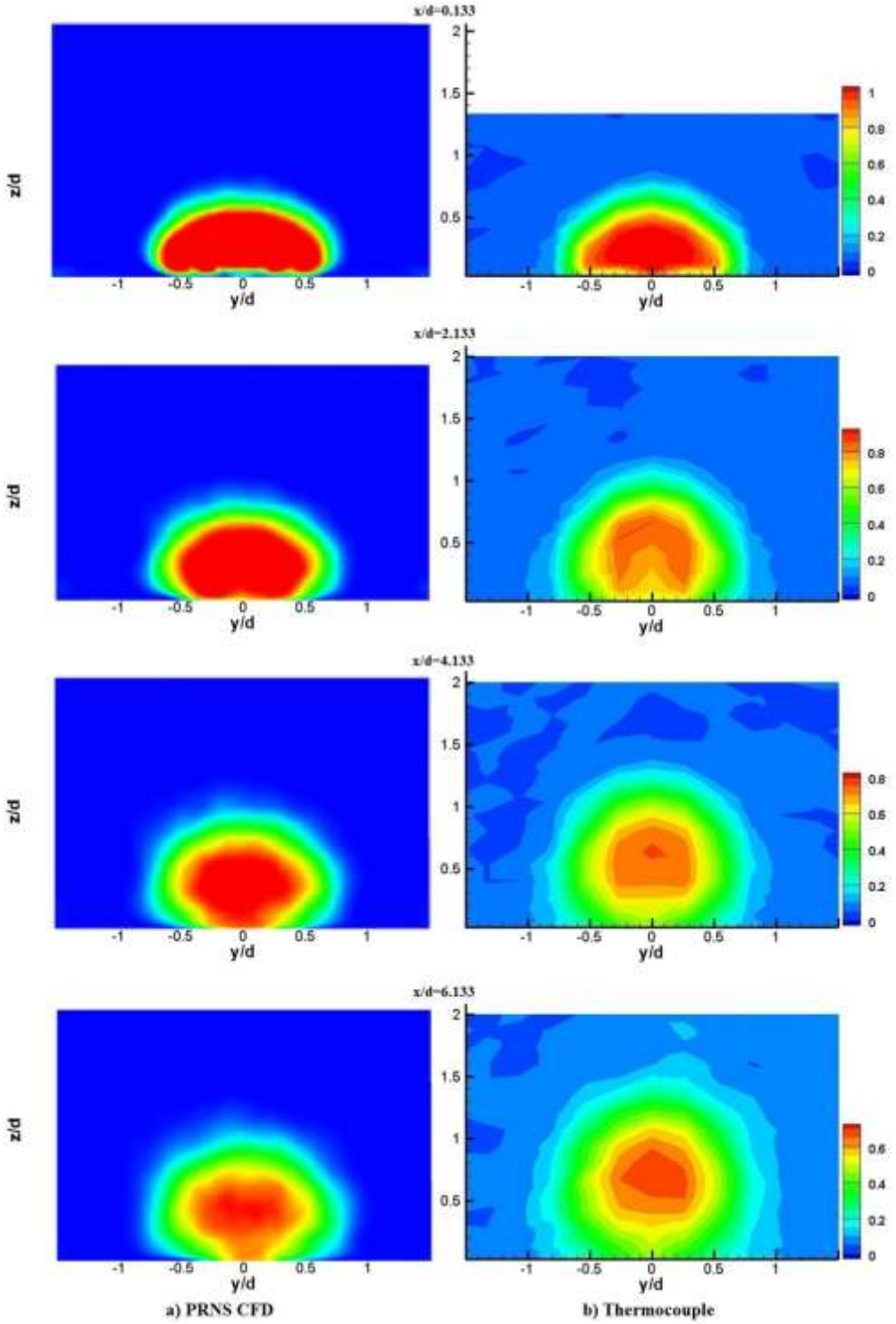


Figure 20.—Effectiveness contours from (a) CFD, (b) thermocouples at planes of constant x/d for M = 1.0, DR = 1.0, Tu = 1.5 percent.

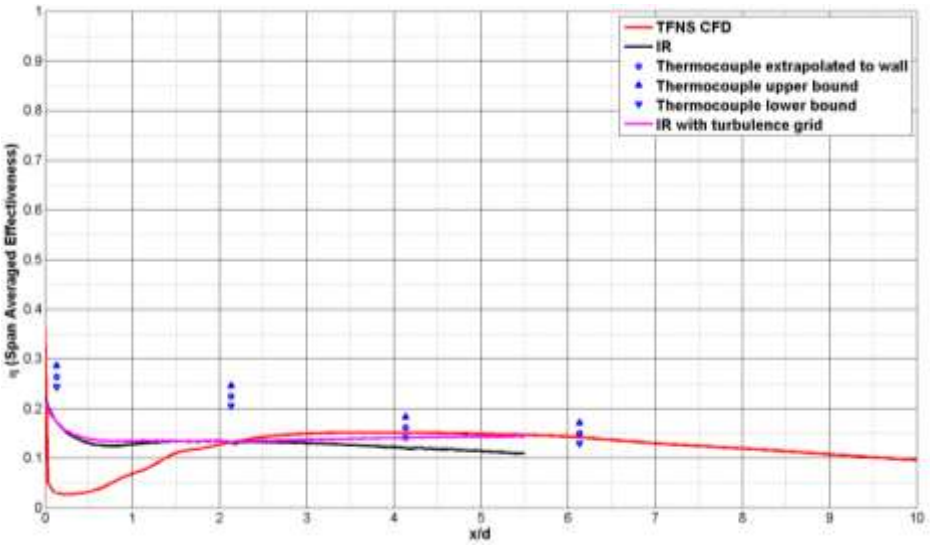


Figure 21.—Spanwise-averaged film effectiveness for M = 1.0, DR = 1.0.

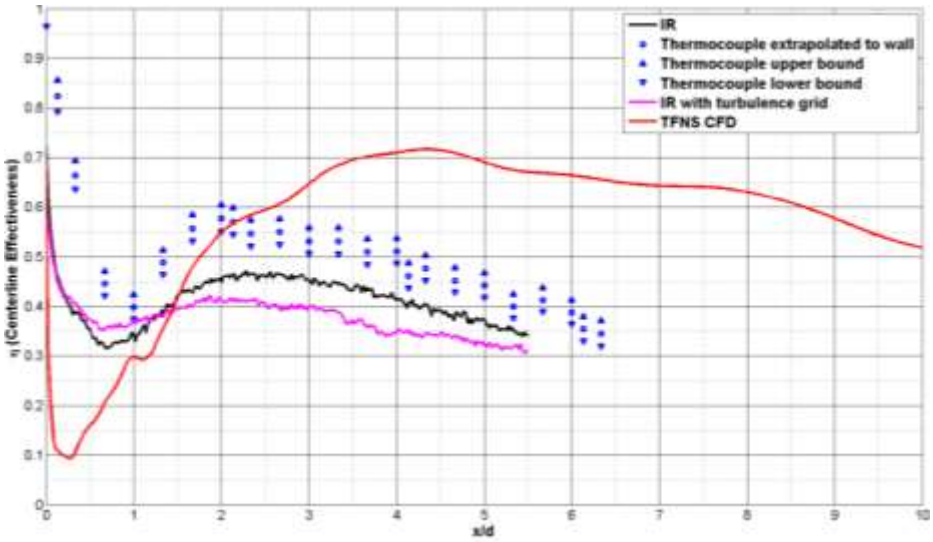


Figure 22.—Centerline film effectiveness for M = 1.0, DR = 1.0.

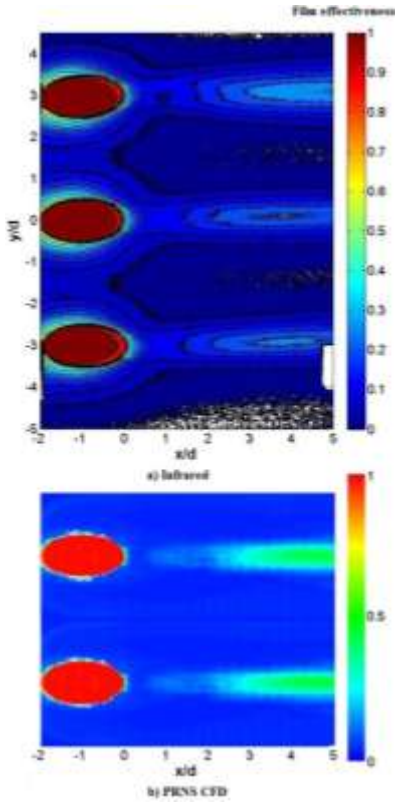


Figure 23.—Film cooling effectiveness from (a) infrared thermography and (b) CFD for M = 1.5, DR = 1.0, Tu = 1.5 percent.

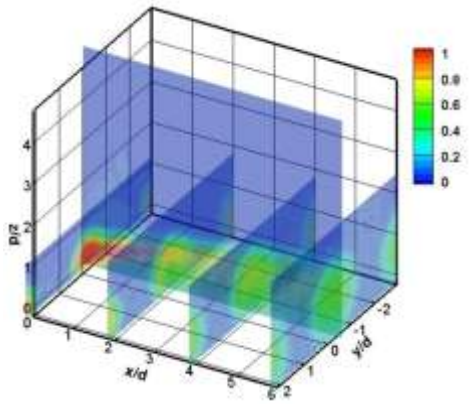


Figure 24.—Film effectiveness from thermocouple surveys for M = 1.5, DR = 1.0, Tu = 1.5 percent.

**Blowing Ratio = 1.5**

Figure 23(a) shows surface effectiveness for a blowing ratio of 1.5 from IR thermography for the low turbulence intensity case (Tu = 1.5 percent). Figure 23(b) shows surface effectiveness from the TFNS simulation. The maximum effectiveness downstream of the hole has dropped to approximately 0.25 and occurs between x/d = 2 and x/d = 3. The jet is completely detached. The CFD shows negligible effectiveness in the region of detachment and this could be due to a lack of prediction of mixing of the coherent hairpin structures with the main flow.

Figure 24 shows effectiveness calculated from thermocouple surveys. Planes at x/d locations of 0.133, 2.133, 4.133, and 6.133 downstream of the cooling hole are shown along with a plane at the centerline. Flow is from left to right along the x/d axis. Figure 25 shows Q-criterion for M = 1.5 from the TFNS simulation. The same features seen

in Figure 12 for M = 0.5 are seen but the jet has now penetrated further into the freestream in the spanwise and vertical direction. The Kelvin Helmholtz vortices persist up to the same downstream extent as in the M = 0.5 case.

Figure 26(a) shows the effectiveness at a plane located at y/d = 0.0 based on TFNS while Figure 26(b) shows effectiveness for the same region from thermocouple surveys. The jet influence extends to approximately z/d = 2.0 at x/d = 1.5 for the thermocouple survey whereas CFD predicts the jet to extend to only z/d = 1.5. The thermocouple survey seems to indicate that the jet is mixing out rapidly and provides fairly constant cooling effectiveness as it travels downstream. The CFD solution has a 'dead zone' of effectiveness between x/d = 0.2 and x/d = 2.0. The coolant is securely carried within the coherent vertical structures and delivered downstream when the coherence is broken. Figure 27 shows contours of effectiveness at planes of constant x/d. The kidney shape seen at x/d = 2.133 is seen to become less resolved at x/d = 4.133 as the jet mixes with the freestream.

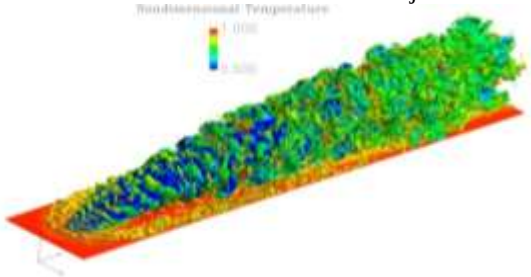

Figure 25.—Isosurfaces of Q-criterion showing Kelvin-Helmholtz instability at M = 1.5, DR = 1.0, Tu = 1.5 percent.

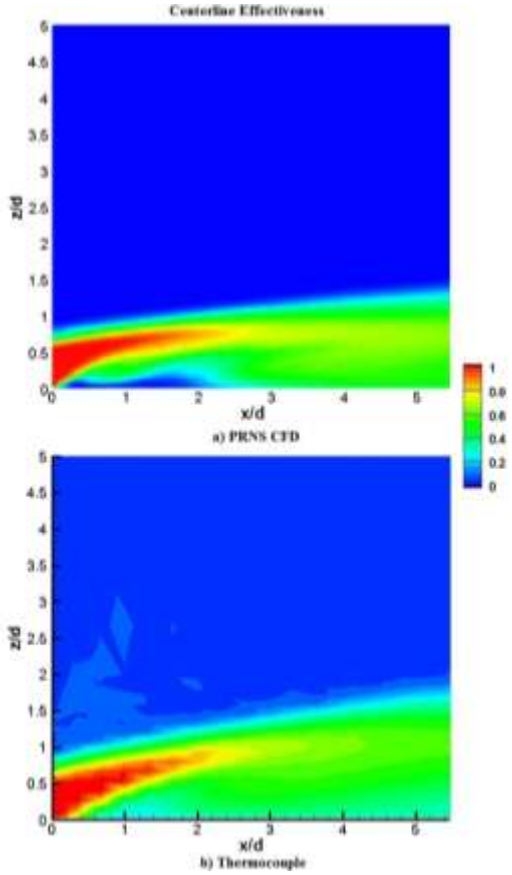


Figure 26.—Centerline effectiveness from (a) CFD and (b) thermocouple at M = 1.5, DR = 1.0, Tu = 1.5 percent.

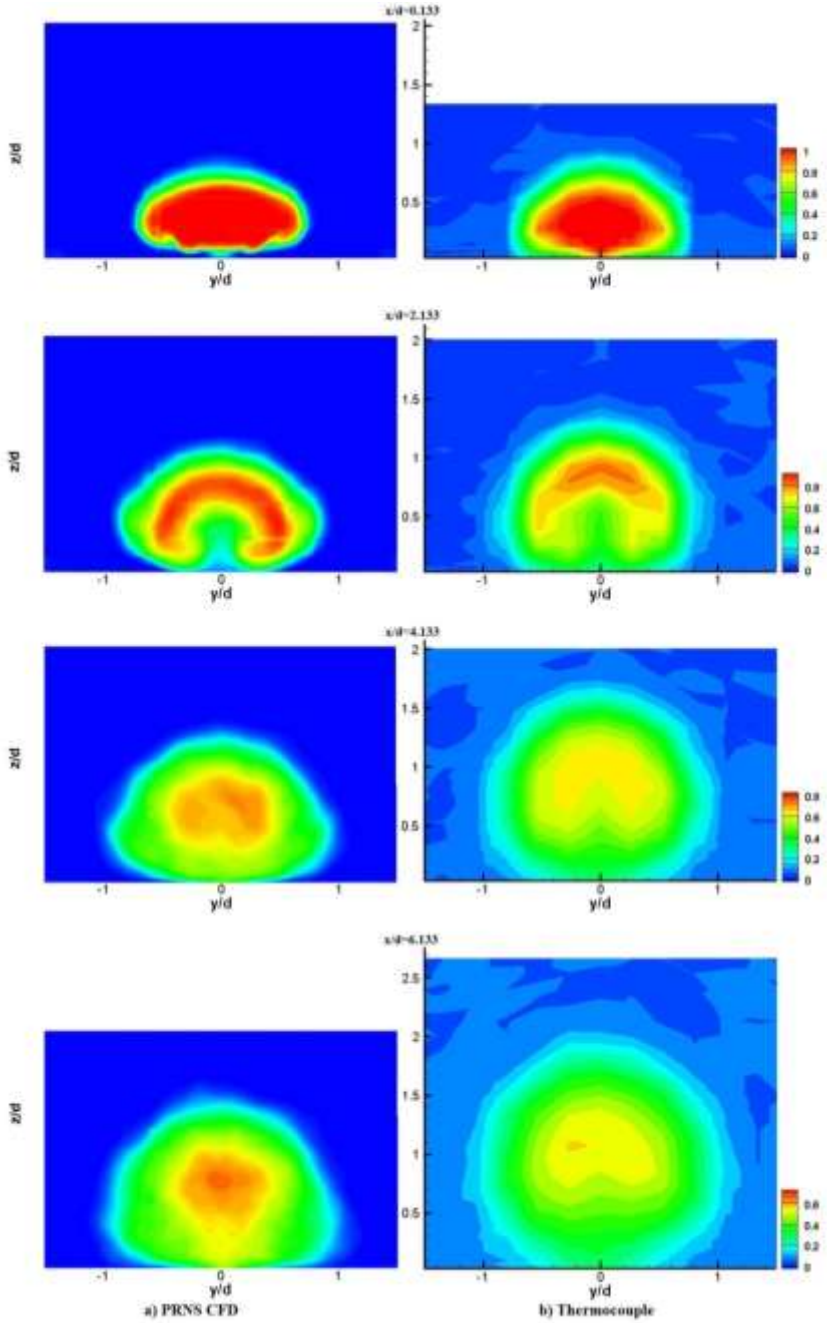


Figure 27.—Effectiveness contours from (a) CFD, (b) thermocouples at planes of constant x/d for M = 1.5, DR = 1.0, Tu = 1.5 percent.

Figures 28 and 29 show span-averaged and centerline effectiveness for M = 1.5 at DR = 1.0. The thermocouple measurements show a consistently higher effectiveness in the near hole region as the Kelvin-Helmholtz vortices are broken up and promote mixing. In the downstream region, the thermocouple results match well with IR. The CFD result starts out over predicting effectiveness because as seen from Figure 12, the hairpin vortices propagate far downstream before they break up. The pink line shows effectiveness from IR thermography with the turbulence grid installed and the trends follow the discussion in the previous section. The centerline effectiveness degrades more rapidly due to the underlying freestream fluid in the near-hole region.

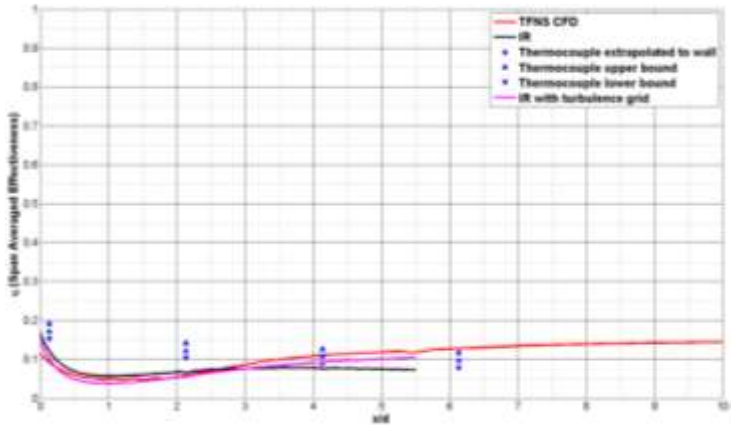


Figure 28.—Spanwise-averaged film effectiveness for M = 1.5, DR = 1.0.

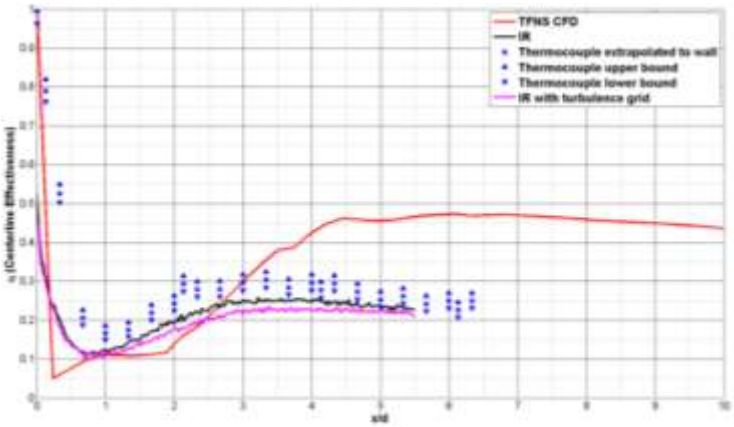


Figure 29.—Centerline film effectiveness for M = 1.5, DR = 1.0.

**Blowing Ratio = 2.0**

Figure 30(a) shows surface effectiveness for a blowing ratio of 2.0 from IR thermography for the low turbulence intensity case (Tu = 1.5 percent). Figure 30(b) shows surface effectiveness from the TFNS simulation. The maximum effectiveness downstream of the hole has dropped to approximately 0.125 and occurs between x/d = 4 and x/d = 5. The jet is completely detached as in the case of M = 1.5. The CFD shows similar trends to those of the M = 1.5 case.

Figure 31 shows effectiveness calculated from thermocouple surveys. Planes at x/d locations of 0.133, 2.133, 4.133, and 6.133 downstream of the cooling hole are shown along with a plane at the centerline. Flow is from left to right along the x/d axis. Figure 32 (a) and (b) show turbulence intensity, *Tu* and nondimensional velocity, $U/U_{inf}$ respectively. Figure 33 shows Q-criterion for M = 1.5 from the TFNS simulation. The same features seen in Figure 12 for M = 0.5 are seen but the jet has now penetrated further into the freestream in the spanwise and vertical direction.

Figure 34(a) shows the effectiveness at a plane located at y/d = 0.0 based on TFNS while Figure 34(b) shows effectiveness for the same region from thermocouple surveys. The jet influence extends to approximately z/d = 2.4 at x/d = 1.5 for the thermocouple survey whereas CFD predicts the jet to extend to only z/d = 1.7. The thermocouple survey seems to indicate that the jet is mixing out rapidly and provides fairly constant cooling effectiveness as it travels downstream. The ‘dead zone’ of effectiveness is now larger and lies between x/d = 0.2 and x/d = 2.5. The coolant is securely carried within the coherent vortical structures and delivered downstream where the coherence is broken. Figures 35 (a) through (d) show turbulence intensity, nondimensional velocity, turbulent shear stress and

integral length scale respectively. Figures 36(a) and (b) show contours of effectiveness at planes of constant x/d from CFD and thermocouple surveys, respectively. Figures 37(a) through (d) show contours of velocity at planes of constant x/d from the hotwire surveys. Figures 38 and 39 show span-averaged and centerline effectiveness for M = 2.0 at DR = 1.0. The thermocouple measurements show a consistently higher effectiveness in the near hole region as the Kelvin-Helmholtz vortices are broken up and promote mixing. In the downstream region, the thermocouple results match well with IR. The TFNS result starts out over predicting effectiveness because as seen from Figure 12, the hairpin vortices propagate far downstream before they break up. Unlike the RANS result (Fig. 35) the TFNS-computed effectiveness follows the trend of the IR thermography data. The RANS simulation predicts complete jet lift-off with little mixing downstream. The pink line shows effectiveness from IR thermography with the turbulence grid installed.

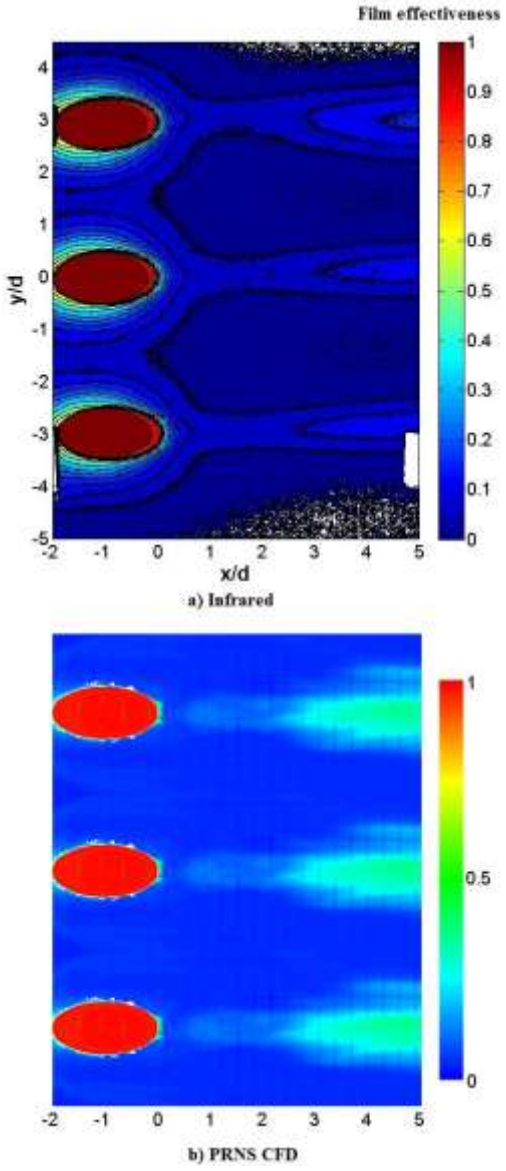


Figure 30.—Film cooling effectiveness from (a) infrared thermography and (b) CFD for M = 2.0, DR = 1.0, Tu = 1.5 percent.

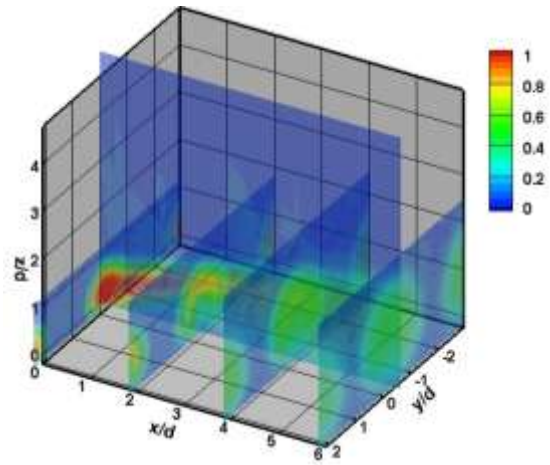


Figure 31.—Film effectiveness from thermocouple surveys for M = 2.0, DR = 1.0, Tu = 1.5 percent.

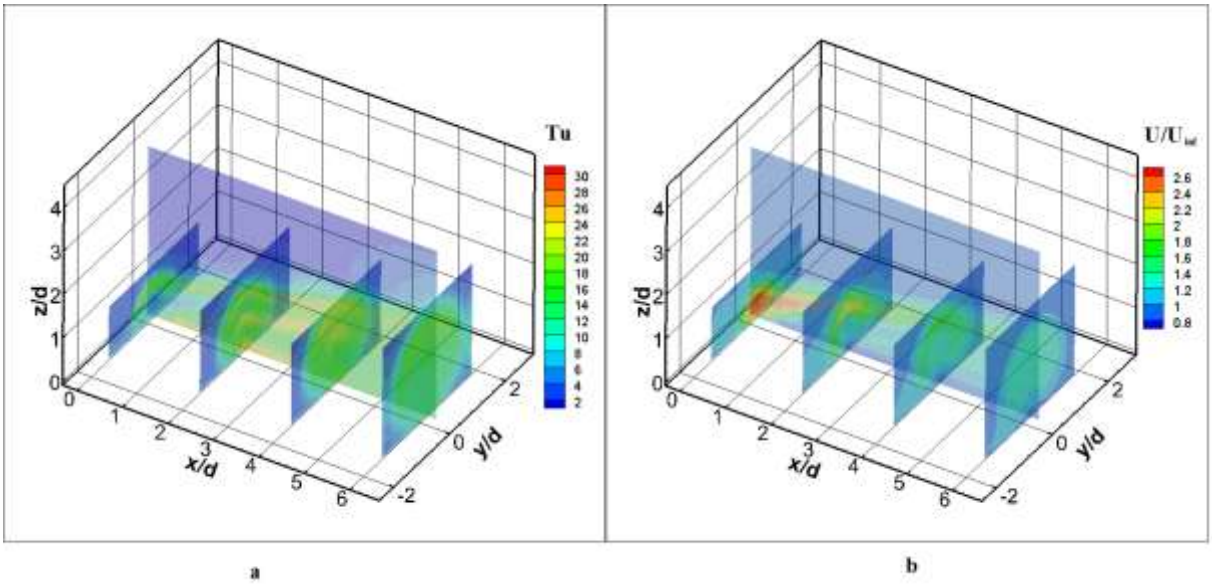


Figure 32.— (a) Turbulence intesity, Tu, and (b) nondimensional velocity magnitude, $U/U_{inf}$ for M = 2.0, DR = 1.0, Tu = 1.5 percent.

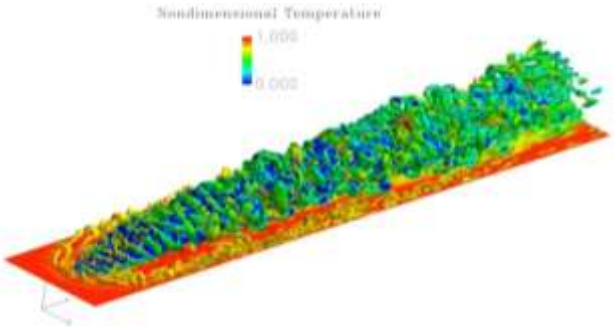


Figure 33.—Isosurfaces of Q-criterion showing at M = 2.0, DR = 1.0, Tu = 1.5 percent.

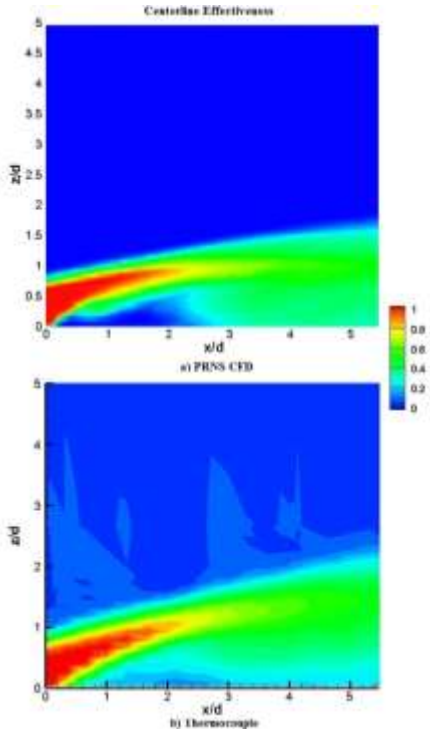


Figure 34.—Centerline effectiveness from (a) CFD and (b) thermocouple at M = 2.0, DR = 1.0, Tu = 1.5 percent.

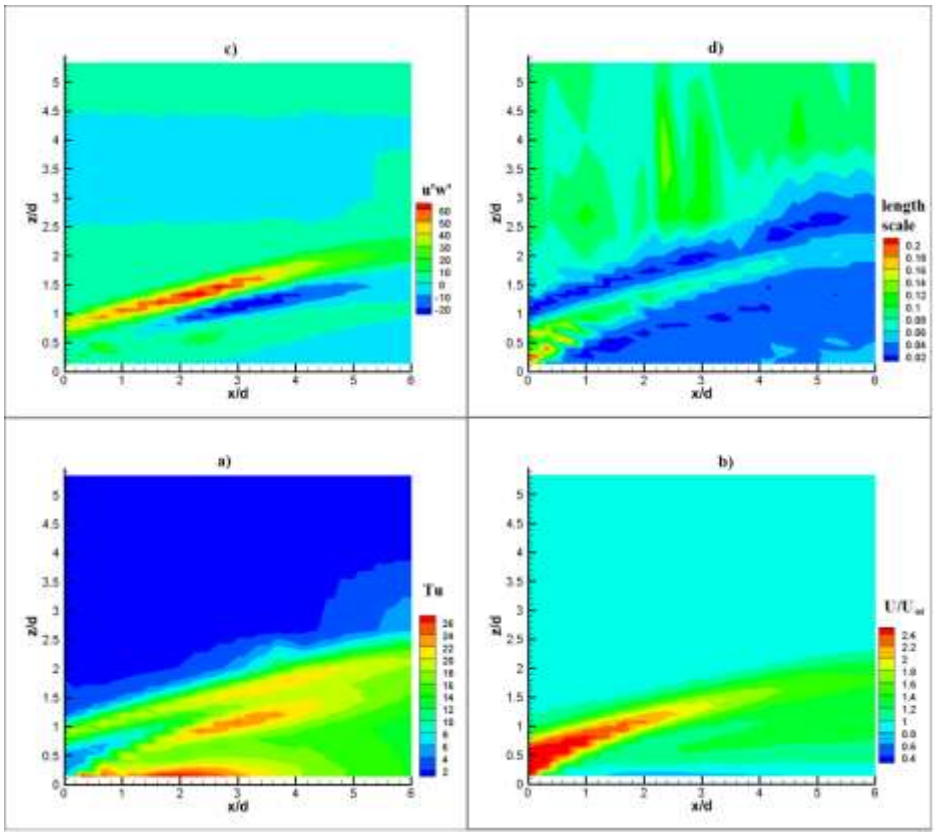


Figure 35.—Centerline contours of (a) turbulence intensity, (b) Nondimensional velocity, (c) turbulent shear stress, (d) integral length scale at M = 2.0, DR = 1.0, Tu = 1.5 percent.

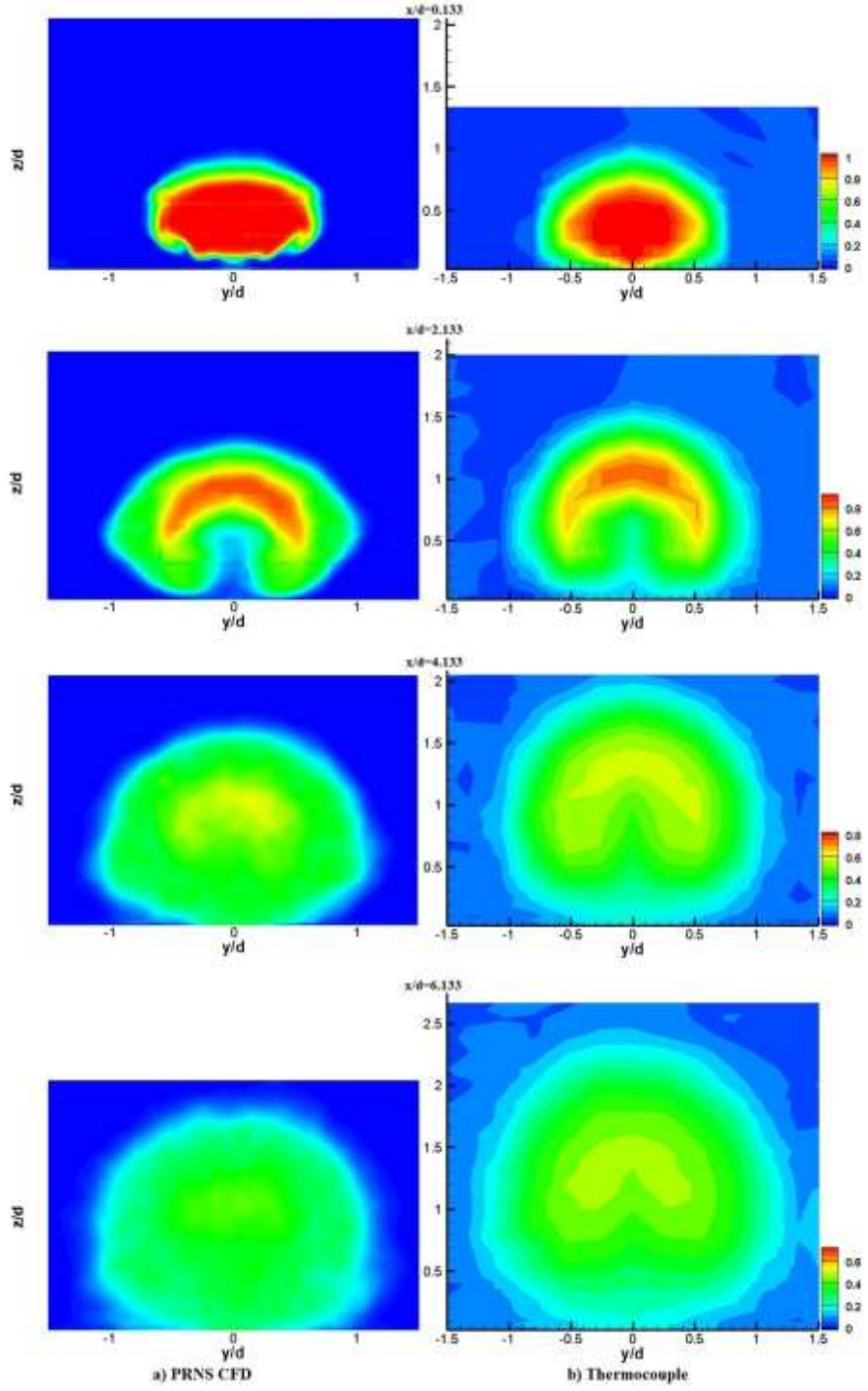


Figure 36.—Effectiveness contours from (a) CFD, (b) thermocouples at planes of constant x/d for M = 2.0, DR = 1.0, Tu = 1.5 percent.

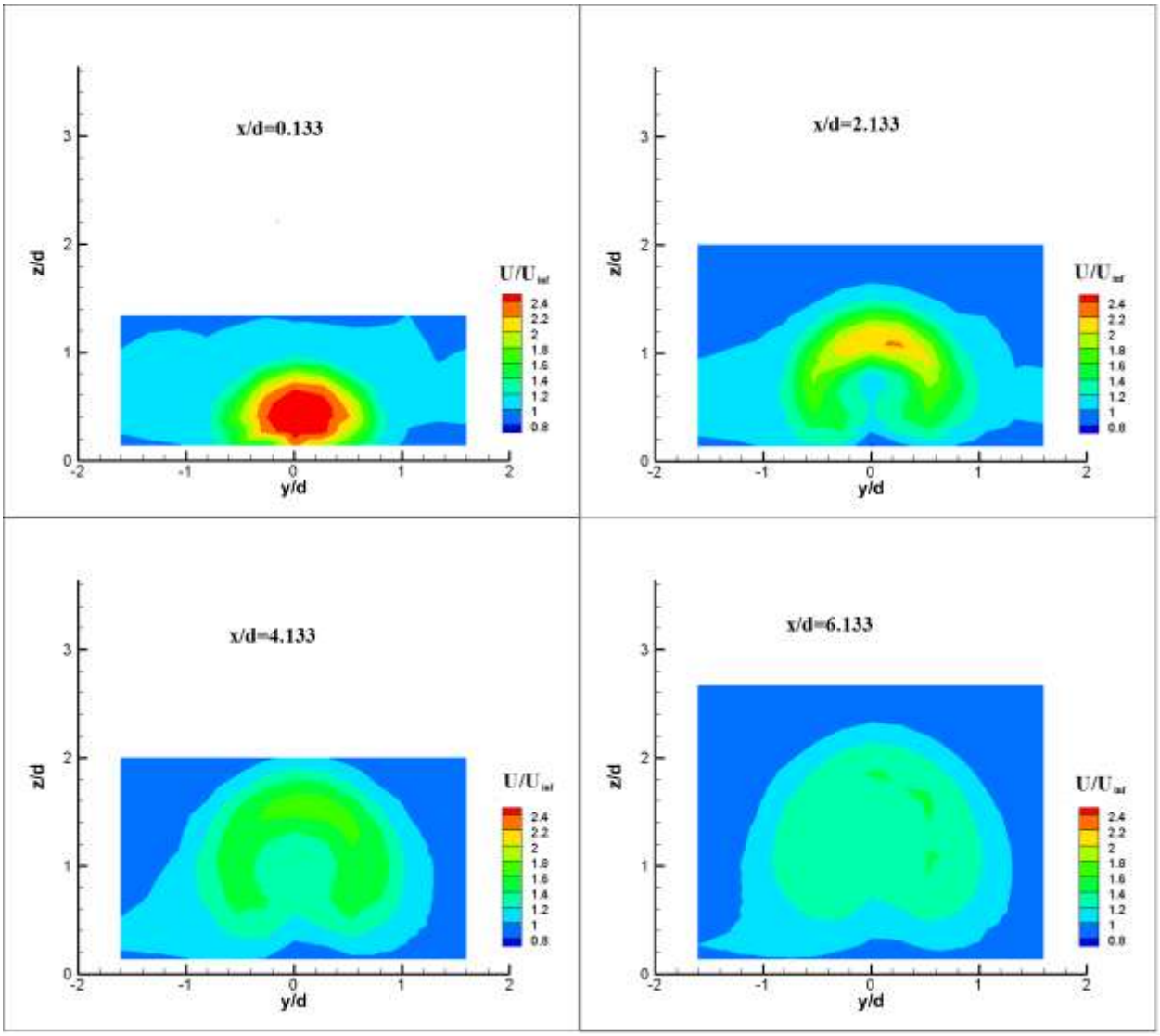


Figure 37.—Ccontours of nondimensional velocity at planes of constant x/d for M = 2.0, DR = 1.0, Tu = 1.5 percent.

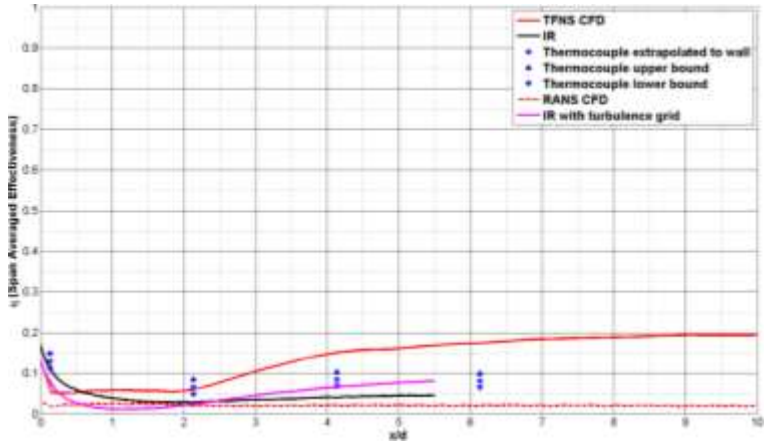


Figure 38.—Spanwise-averaged film effectiveness for M = 2.0, DR = 1.0.

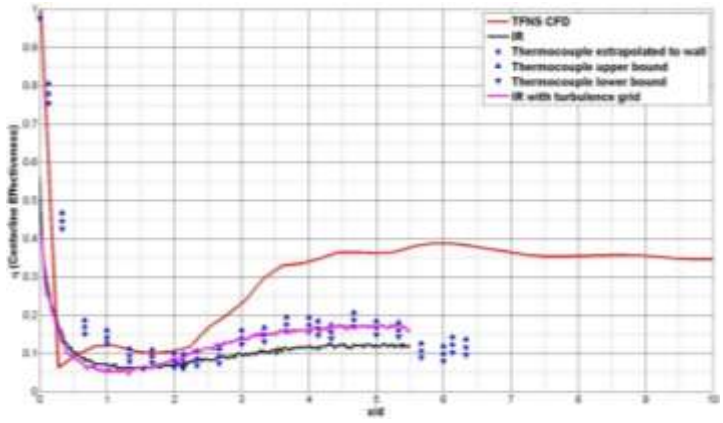


Figure 39.—Centerline film effectiveness for M = 2.0, DR = 1.0.

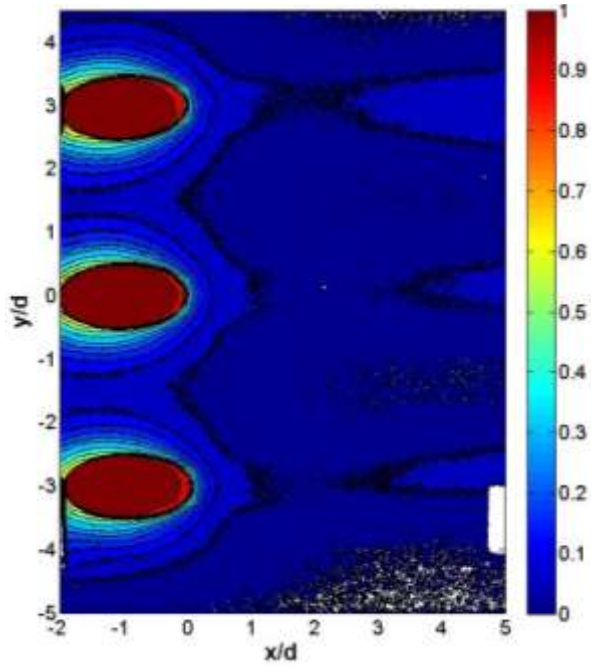


Figure 40.—Film cooling effectiveness computed from infrared thermography for M = 2.5, DR = 1.0, Tu = 1.5 percent.

**Blowing Ratio = 2.5**

Figure 40 shows surface effectiveness for a blowing ratio of 2.5 from IR thermography for the low turbulence intensity case (Tu = 1.5 percent). The maximum effectiveness downstream of the hole has dropped to approximately 0.06 and occurs downstream of x/d = 5. Figures 41 and 42 show span-averaged and centerline effectiveness for M = 2.5 at DR = 1.0 from infrared thermography.

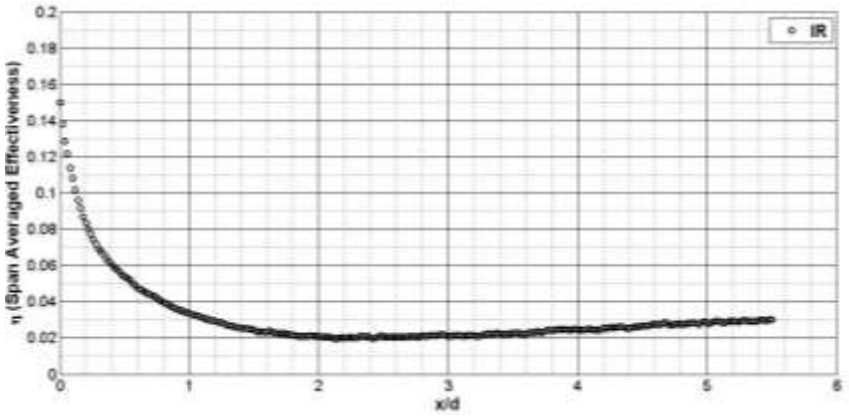


Figure 41.—Spanwise-averaged film effectiveness for M = 2.5, DR = 1.0, Tu = 1.5 percent.

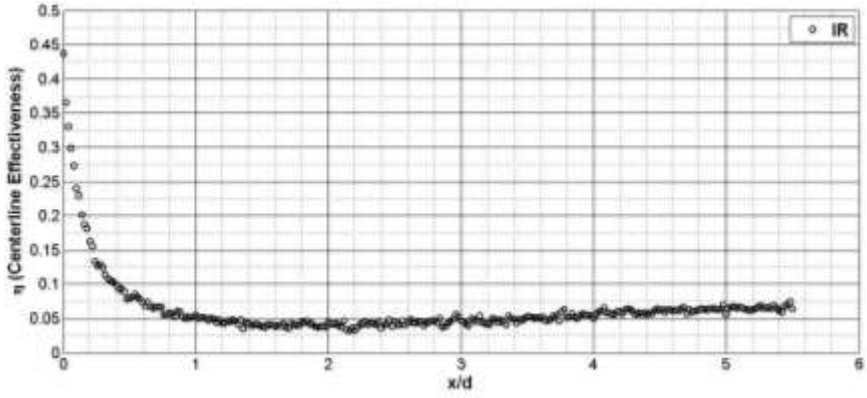


Figure 42.—Centerline film effectiveness for M = 2.5, DR = 1.0, Tu = 1.5 percent.

**VI. Comparison with Prior Work**

This section compares the results from the present study to data found in the literature. In order to enable better comparison of the varying configurations, the momentum flux ratio, I, (the square of blowing ratio divided by density ratio) is used to compare cases with different density ratios. For cases where blowing ratio is not the same as for the present study, the blowing ratio is noted in addition to the momentum flux ratio. Figures 43 and 45 show centerline effectiveness for I = 0.25, and 1.0, respectively. Figures 44, 46, 47, and 48 show span-averaged effectiveness for I = 0.25, 1.0, 2.25, and 4.0, respectively. Unless otherwise specified, the angle of inclination of the holes to the freestream direction is 30°. The data presented here was extracted from online publications using a plot digitizer.

Dhungel (Ref. 32) studied the effect of sister hole or 'anti-vortex' configurations and used round holes inclined at 30° as the baseline. The holes had P/D = 3.0 and L/D = 5.0. The Reynolds number based on hole diameter was 11000 and the freestream turbulence intensity was 2 percent. The holes were fed through a plenum. Johnson et al. (Ref. 33) used PIV and PSP to investigate film cooling from a row of circular holes inclined at 30° to the freestream. The hole spacing was 10 which is fairly large and is expected to lead to non-interacting coolant jets. The L/D was 6 and the turbulence intensity was under 1 percent. Density ratios of 0.97, 1.0, and 1.53 and blowing ratios in the range 0.4 to 1.7 were studied. An attempt was made to collapse data based on density ratios, momentum ratios and blowing ratios. Lawson and Thole (Ref. 34) conducted an experiment to study the effect of deposition on film cooling effectiveness due to holes angled at 30°. Turbulence intensities of 4.6 and 12.3 percent were considered. Holes were spaced three hole diameters apart with L/D = 3.0. Blowing ratios of 0.49, 0.73, and 1.01 were studied with nominal density ratio of 1.06. Rallabandi et al. (Ref. 35) investigated the effect of an upstream step on flat plate effectiveness. They used simple angled, compound angled, cylindrical and fan-shaped holes. Hole inclinations, $\alpha$, of 30° and 45° were used with P/D = 3 and L/D = 7.5. The range of blowing ratios was 0.3 to 1.5 with unit density ratio. Turbulence intensity is estimated to be below 0.5 percent.

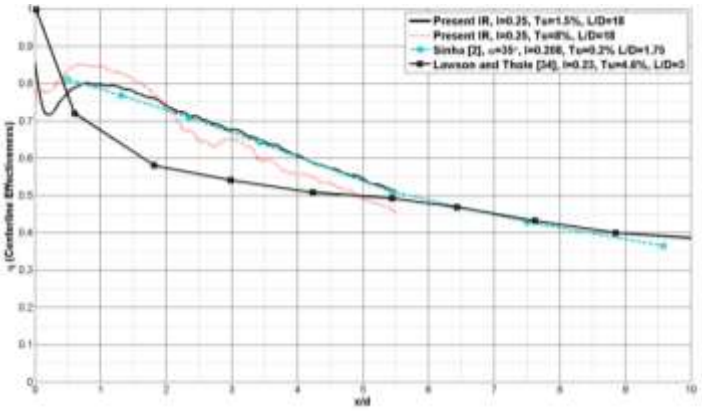


Figure 43.—Centerline effectiveness for I = 0.25 (corresponds to DR = 1.0, M = 0.5 in present study).

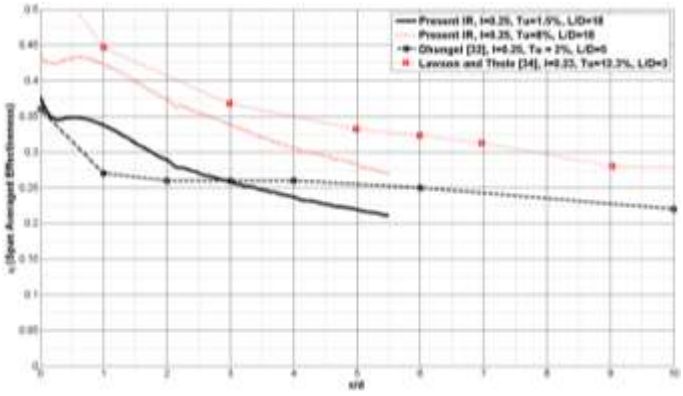


Figure 44.—Span-averaged effectiveness for I = 0.25 (corresponds to DR = 1.0, M = 0.5 in present study).

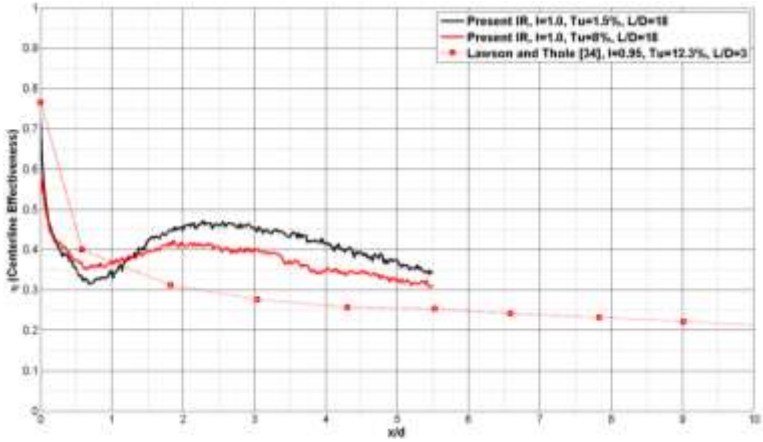


Figure 45.—Centerline effectiveness for I = 1.0 (corresponds to DR = 1.0, M = 1.0 in present study).

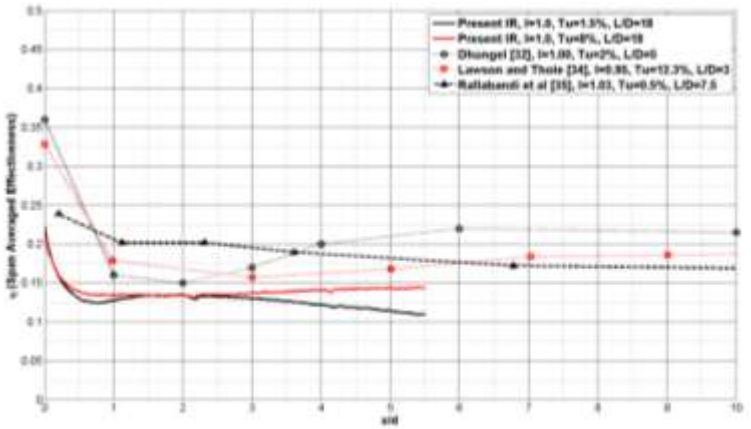


Figure 46.—Span-averaged effectiveness for I = 1.0 (corresponds to DR = 1.0, M = 1.0 in present study).

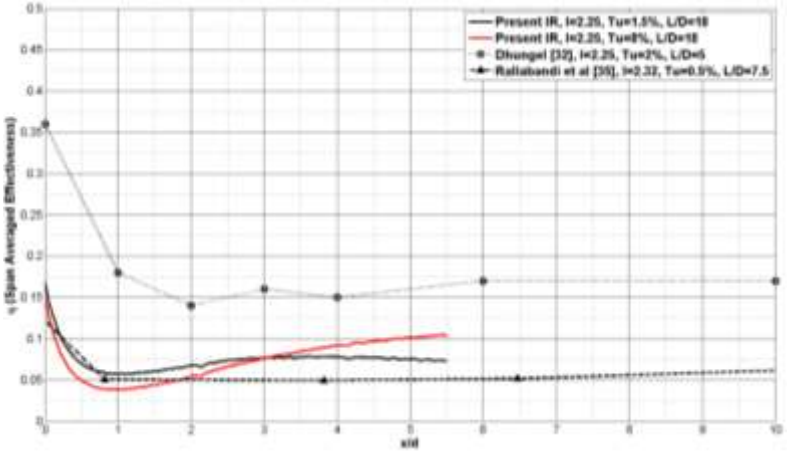


Figure 47.—Span-averaged effectiveness for I = 2.25 (corresponds to DR = 1.0, M = 1.5 in present study).

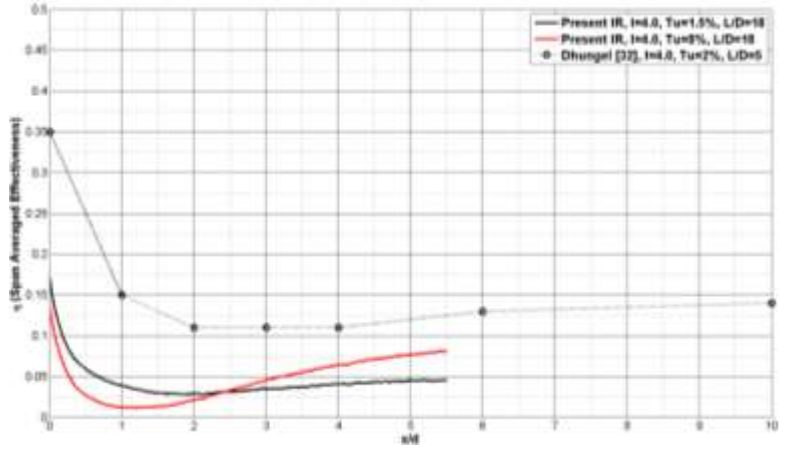


Figure 48.—Span-averaged effectiveness for I = 4.0 (corresponds to DR = 1.0, M = 2.0 in present study).

## VII. Conclusions

Infrared thermography of a flat plate cooled by long holes inclined at 30° to the freestream was conducted. The film effectiveness obtained from IR thermography was found to match well with thermocouple surveys and is thought to have less uncertainty than the thermocouple measurements. Kelvin Helmholtz structures were observed in the Time-Filtered Navier Stokes simulations that appeared to persist far downstream of the cooling hole. The breakup of these coherent structures gives improved effectiveness downstream of the hole especially for high blowing ratio. However, the delayed breakup predicted by CFD results in the predicted effectiveness being far higher than that shown by IR thermography. It also appears that thermocouple surveys are possibly influencing the rapid mixing of the jet at high blowing ratios causing a fairly constant level of span averaged effectiveness. Furthermore, the effectiveness computed by the thermocouples is at a height of $z/d = 0.03$ above the surface. Thus the thermocouple yields consistently higher effectiveness than infrared thermography. The surface effectiveness predicted by CFD does follow the same trend as the effectiveness deduced from the infrared imaging. This could imply that modification of the filtering parameter or increased refinement downstream of the hole could yield more satisfactory results. It is also necessary to look at the turbulent stresses in the near-hole region to determine the reason for the coherence of the Kelvin Helmholtz structures. Results from hotwire surveys will be analyzed and compared to the Reynolds stresses predicted by CFD.


### Acknowledgements

This work was performed under the Fixed Wing Project of the Fundamental Aeronautics program at the NASA Glenn Research Center.


### References


1. Bogard, D., and Thole, K., 2006, "Gas Turbine Film Cooling," Journal of Propulsion and Power, 22(2), 249–270, DOI:10.2514/1.18034.
2. Sinha, A.K., Bogard, D.G., and Crawford, M.E., 1991, "Film-Cooling Effectiveness Downtream of a Single Row of Holes with Variable Density Ratio," Journal of Turbomachinery, Vol. 113, pp. 442-449.
3. Pedersen, D.R., Eckert, E., and Goldstein, R., "Film Cooling with Large Density Differences Between the Mainstream and the Secondary Fluid Measured by the Heat-MassTransfer Analogy," Journal of Heat Transfer, Vol. 99, Q18 1977, pp. 620–627.
4. Bons, J.P., Rivir, R.B., Mac, A., Charles D., "The Effect of High Freestream Turbulence on Film Cooling Effectiveness," WL-TR-96-2097, 13-16 June 1994.
5. Mayhew, J., Baughnb, J., Byerleyc, A., "The effect of freestream turbulence on film cooling adiabatic effectiveness," International Journal of Heat and Fluid Flow, Volume 24, Issue 5, October 2003, pp. 669-679.
6. Lutum, E., and Johnson, B.V., 1998, "Influence of the Hole Length to Diameter Ratio on Film Cooling With Cylindrical Holes," ASME J. Turbomachinery, 121, pp. 209–216.
7. Thurman, D.G., El-Gabry, L.A., Poinsatte, P.E., and Heidmann, J.D., 2011, "Turbulence and Heat Transfer Measurement in and Inclined Large Scale Film Cooling Array – Part II, Temperature and Heat Transfer Measurements," ASME paper GT2011-46498, ASME Turbo Expo 2011, Vancouver.
8. Han, J.C. and Rallabandi, A.P., 2010, "Turbine Blade Film Cooling Using PSP Technique," Frontiers Heat Mass Transfer, 1 (1), pp. 1–21.
9. Papell, S.S., Graham R.W., Cageao, R.P., "Influence of coolant tube curvature on film cooling effectiveness as detected by infrared imagery," NASA Technical Paper 1546, November 1979.
10. Baldauf, S., A. Schulz, and S. Wittig. "High-resolution measurements of local effectiveness from discrete hole film cooling," Journal of Turbomachinery Vol. 123.4, 2001, pp. 758-765.
11. Ekkad, S. v., Ou, S., and Rivir B.R., "A Transient Infrared Thermography Method for Simultaneous Film Cooling Effectiveness and Heat Transfer Coefficient Measurements From a Single Test," Journal of Turbomachinery, Vol. 126, October 2004, pp. 597-603.
12. Wright, L., McClain, S., and Clemenson, M., "Effect of Density Ratio on Flat Plate Film Cooling With Shaped Holes Using PSP," Journal of Tubomachinery, Vol. 133 October 2011, pp. 041011-1 – 041011-11.
13. Sgarzi, O., and Leboeuf, F., 1997, "Analysis of Vortices in Three-Dimensional Jets Introduced in a Cross-Flow Boundary Layer," ASME Paper No. 97-GT- 517.

14. El-Gabry, L., Heidmann, J. and Ameri, A.A., "Numerical Analysis of Fill Cooling at High Blowing Ratio," NASA/TM—2009-215517.
15. X. Guo, X., Schröder, W., Meinke, M., "Large-eddy simulations of film cooling flows," Computers & Fluids 35 (2006) 587–606.
16. Tyagi, M. and Acharya, S., 2003, "Large eddy simulation of film cooling flow from an inclined cylindrical jet," *ASME Journal of Turbomachinery*, Vol. 125, pp. 734-742.
17. Fujimoto, S. "Large Eddy Simulation of Film Cooling Flows Using Octree Hexahedral Meshes," GT2012-70090 June 11-15, 2012, Copenhagen, Denmark.
18. Y. Peet and S.K. Lele (2008) "Computational Framework for Coupling Compressible and Low Mach Number Codes," *AIAA Journal*, vol. 46, No. 8, pp. 1990-2001.
19. Wilcox, D. C., 1994, "Simulation of Transition With a Two-Equation Turbulence Model," AIAA Journal, Vol. 32, No. 2, pp. 274-255.
20. Steinthorsson, E., Liou, M.S., and Povinelli, L.A., 1993, "Development of an Explicit Multiblock/Multigrid Flow Solver for Viscous Flows in Complex Geometries," AIAA-93-2380; also NASA TM-106356.
21. Liu, N.-S., and Shih, T.-H., "Turbulence Modeling for Very Large-Eddy Simulation," *AIAA Journal*, Vol. 44, No. 4, 2006, pp. 687-697.
22. Shih, T.-H., and Liu, N.-S., 2009, "Modeling of Internal Reacting Flows and External Static Stall Flows Using RANS and PRNS," Flow, Turbulence and Combust (2008) 81:279-299.
23. Shih, T.H., and Liu, N.S., A Nonlinear Dynamic Subscale Model for PRNS/VLES of Internal Combustor Flows, AIAA-2009-0467.
24. Liu, Nan-Suey, Wey, Thomas, Shih, Tsan-Hsing, 2013, "Time-Filtered Navier-Stokes Approach and Emulation of Turbulence-Chemistry Interaction," AIAA 2013-0707, 51st AIAA Aerospace Sciences Meeting Including the New Horizons Forum and Aerospace Exposition. January.
25. Davidson, L., and Peng, S.H., "Hybrid LES-RANS modeling: a one-equation SGS model combined with a $k-\omega$ model for predicting recalculating flows," International Journal for Numerical Methods in Fluids, Vol. 43, 2003, pp. 1003-1018.
26. Larsson, J., Lien, F.S. and Yee, E., "The artificial buffer layer and the effect of forcing in hybrid LES/RANS," International Journal of Heart and Fluid Flow, Vol. 28, 2007, pp. 1443-1459.
27. Spalart, P.R., Jou, W.H., and Allmaras, S.R., "Comments on the feasibility of LES for wings and on a hybrid RANS/LES approach," Advances in DNS/LES, 1997, Greyden Press.
28. Fasel, H.F., and von Terzi, D.A. and Sandberg, R.D., "A methodology for simulating compressible turbulent flows," Journal of Applied Mechanics, Vol. 73, pp. 405-412.
29. Hunt, J.C.R., Wray, A. & Moin, P. 1988, "Eddies, stream, and convergence zones in turbulent flows," Center for Turbulence Research Report CTR-S88.
30. Brown, A. and Saluja, C.L., "Film Cooling From a Single Hole and a Row of Holes of Variable Pitch to Diameter Ratio". Int. J. Heat and Mass Transfer, Vol. 22, pp. 525-533, 1979.
31. Dhungel, A., "Film Cooling From A Row Of Holes Supplemented With Anti Vortex Holes," M.S. Thesis, Louisiana State University, 2007.
32. Johnson, B., Zhang, K., Tian W. and Hu, Hui, "Experimental study of film cooling effectiveness by using PIV and PSP techniques," AIAA 2013-0603, Proceedings of the AIAA Aerosciences Meeting, 07-10 January 2013, Grapevine Texas.
33. Lawson, S.A., and K.A. Thole. "Effects of simulated particle deposition on film cooling," Journal of Turbomachinery 133.2 (2011): 021009.
34. Rallabandi, A.P., Grizzle, J., Han, J-C. 2011. "Effect of Upstream Step on Flat Plate Film-Cooling Effectiveness Using PSP," Journal of Turbomachinery. Vol. 133, pp. 041024-1–8.